Comput Mech (2010) 46:471–493
DOI 10.1007/s00466-010-0490-4

ORIGINAL PAPER

Natural element analysis of the Cahn–Hilliard phase-field model

Amirtham Rajagopal · Paul Fischer · Ellen Kuhl · Paul Steinmann

Received: 27 November 2009 / Accepted: 4 March 2010 / Published online: 7 April 2010

Abstract We present a natural element method to treat higher-order spatial derivatives in the Cahn–Hilliard equation. The Cahn–Hilliard equation is a fourth-order nonlinear partial differential equation that allows to model phase separation in binary mixtures. Standard classical $\mathcal{C}^0$-continuous finite element solutions are not suitable because primal variational formulations of fourth-order operators are well-defined and integrable only if the finite element basis functions are piecewise smooth and globally $\mathcal{C}^1$-continuous. To ensure $\mathcal{C}^1$-continuity, we develop a natural-element-based spatial discretization scheme. The $\mathcal{C}^1$-continuous natural element shape functions are achieved by a transformation of the classical Farin interpolant, which is basically obtained by embedding Sibsons natural element coordinates in a Bernstein–Bézier surface representation of a cubic simplex. For the temporal discretization, we apply the (second-order accurate) trapezoidal time integration scheme supplemented with an adaptively adjustable time step size. Numerical examples are presented to demonstrate the efficiency of the computational algorithm in two dimensions. Both periodic Dirichlet and homogeneous Neumann boundary conditions are applied. Also constant and degenerate mobilities are considered. We demonstrate that the use of $\mathcal{C}^1$-continuous natural element shape functions enables the computation of topologically correct solutions on arbitrarily shaped domains.

Keywords Cahn–Hilliard equation · Fourth-order diffusion · Phase separation · Higher-order continuity · Natural element method

A. Rajagopal · P. Fischer · P. Steinmann (✉)
Chair of Applied Mechanics, University of Erlangen Nuremberg, 91058 Erlangen, Germany
e-mail: steinmann@ltm.uni-erlangen.de

A. Rajagopal
e-mail: rajagopal@ltm.uni-erlangen.de

P. Fischer
e-mail: paul.fischer@ltm.uni-erlangen.de

E. Kuhl
Departments of Mechanical Engineering, Bioengineering and Cardiothoracic Surgery, Stanford University, Stanford, CA 94305, USA
e-mail: ekuhl@stanford.edu

1 Introduction

The understanding of phase separation is extremely crucial not only when in understanding the formation of natural materials, for example in geophysics, but also when designing novel highly functional materials, for example in process engineering, chemistry, physics, and material sciences. Phase separation phenomena are characterized through a multicomponent mixture that spontaneously separates and forms domains pure in each component. Usually, phase separation is induced by cooling down the mixture as the free energy reaches a critical value.

The Cahn–Hilliard equation is widely used to characterize the kinetics and morphology evolution of phase separation in a mathematical sense. Typical examples are multiphase fluid flow [4,10], image processing [8], mineral exsolution and growth [21], biological applications [20], and polymer science [31], just to name a few. Phase separation or spinodal decomposition requires uphill diffusion in which material moves against the concentration gradients and is driven by gradients in the chemical potential. These processes are governed by the competition of two energies, a local configurational energy, expressed in terms of one of the concentrations, and a surface energy, expressed in terms of concentration gradients. Initial stages of the phase separation process minimize

the configurational energy by driving the local concentrations into the two valleys of the energy potential which can be associated with the pure phases. Later stages minimize the surface energy by larger single-phase domains successively absorbing smaller pure phase regions, minimizing the interface area between the individual phases.

Computational solutions to the Cahn–Hilliard equation are extremely challenging for multiple reasons. First, initial phase separation and surface energy minimization take place on different time scales, requiring an adaptive time stepping scheme. Second, the configurational energy is a highly nonlinear function in the concentration, requiring an iterative solution procedure when utilizing unconditionally stable implicit time integration schemes. Third, and probably most critical, the surface energy is associated with fourth-order gradients, requiring a higher-order interpolation of the numerical discretization scheme.

Phase separation phenomena have conventionally been studied through sharp interface models and phase field models. Sharp interface models require the solution of moving boundaries. The partial differential equations for each phase are solved individually, satisfying the energy balance and the Gibbs Thompson equation coupled with the interface boundary condition, e.g., the Stefan condition, between the individual phases. Typical computational representatives along these lines are front tracking methods [28] and level-set-based interface capturing methods [22,24].

In this sense, phase field methods are probably more straightforward and therefore more widely used. For simple regular non-moving domains, classical finite different schemes [5,15] or spectral approximation schemes [13,19] provide excellent solutions. In the case of complex non-constant domains, however, finite element schemes seem to be an unavoidable choice [1,6,9]. The presence of fourth-order operators requires basis functions that are piecewise smooth and globally $\mathcal{C}^1$-continuous. There are very few finite elements formulations that possess $\mathcal{C}^1$-continuity while at the same time being applicable to complex geometries [16]. On arbitrary unstructured meshes, $\mathcal{C}^1$-continuous spaces of complete piecewise polynomials typically require an undesirable increase of the polynomial degree to ensure optimal accuracy. To elegantly solve the issue of constructing conforming function spaces on non-conforming adaptively refined meshes, a powerful novel algorithm has been proposed, in which each element is treated as a piecewise-polynomial macroelement [25]. To circumvent these limitations and conceptual complexities, the fourth-order Cahn–Hilliard equation can be rephrased to yield two second-order equations, reducing the continuity requirement to $\mathcal{C}^0$, and introducing the local and nonlocal concentrations as primary unknown at each node [21,29]. Alternatively, discontinuous Galerkin methods have been proposed in which continuity at internal element boundaries is enforced in a weak sense inspired by the interior penalty method [30]. Recently, meshless methods [32] and isogeometric analysis [16,17] have been proposed to solve the Cahn–Hilliard equation. The latter approach has strong similarities with the higher-order natural element method [26], which we have recently successfully applied to solve the fourth-order differential equations of gradient elasticity [14,23]. This has inspired the design of a natural element scheme for the Cahn–Hilliard equation.

This manuscript is organized as follows. To set the stage, a brief derivation of the Cahn–Hilliard equation is given in Section 2. In Sect. 3, we illustrate the basic features of the natural element method and demonstrate the derivation of its $\mathcal{C}^0$- and $\mathcal{C}^1$-continuous shape functions. Details related to the numerical implementation of the $\mathcal{C}^1$-continuous natural element method for the Cahn–Hilliard equation are discussed in Sect. 4. In Sect. 5, we demonstrate the basic features of the proposed algorithm in terms of selected benchmark problems. A critical discussion concludes this manuscript in Sect. 6.

2 The Cahn–Hilliard equation

Let us consider a binary mixture of two constituents with c and $[\,1-c\,]$ as their respective concentrations. The concentration c satisfies the condition $0 \leq c \leq 1$. Pure phases are obtained for $c = 0$ and $c = 1$. Let the binary mixture occupy an open, simply connected region in space, $\Omega \subset \mathbb{R}^{\mathrm{d}}$, with dimension d = 1, 2, or 3. According to the Cahn–Hilliard equation, the temporal evolution $\dot{c}$ of the concentration c is governed by the following diffusion equation,

$$\dot{c} = -\nabla \cdot \boldsymbol{j} \quad \text{with } \boldsymbol{j} = -M\,\nabla\mu \tag{1}$$

where the flux of concentrations $\boldsymbol{j}$ is driven by gradients in the chemical potential $\nabla\mu$ weighted by the mobility $M > 0$,

$$\dot{c} = \nabla \cdot (M\,\nabla\mu). \tag{2}$$

The chemical potential μ can be expressed through the variational derivative, $\mu = \delta_c(\Psi^c) = \partial_c(\Psi^c) - \nabla\cdot(\partial_{\nabla c}(\Psi^c))$, in terms of the free energy density $\Psi^c = \Psi^{\mathrm{con}}(c) + \Psi^{\mathrm{sur}}(\nabla c)$. Here, $\Psi^{\mathrm{con}}(c)$ denotes the configurational energy parameterized in terms of the local concentration c. This is given by

$$\Psi^{\mathrm{con}} = RT[c\ \log c + [1-c]\ \log(1-c) + 2\theta\, c\,[1-c]]. \tag{3}$$

In the above Eq. (3), R is the gas constant expressed in units of energy per Kelvin per volume, T_c is the critical temperature, i.e., the temperature at which the two phases attain the same composition, T is the absolute temperature in Kelvin and $\theta = T_c\,/\,T$ is a dimensionless number which represents the ratio between the critical and the absolute temperatures

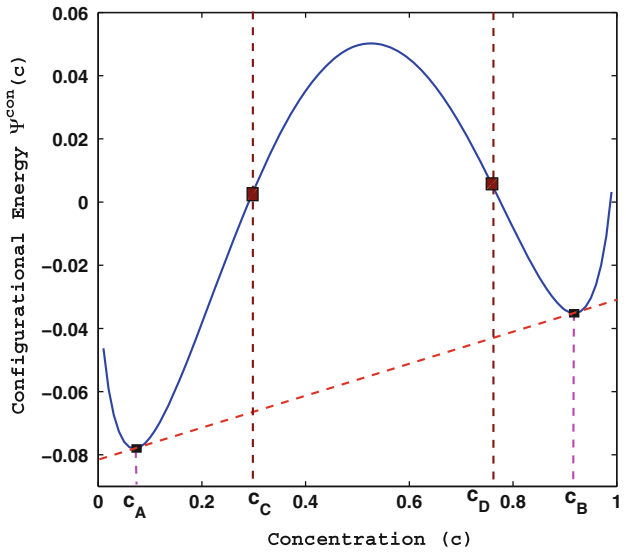

Fig. 1 Typical double-well shape of the non-convex configurational energy Ψ^{con} as a function of the concentration c. The spinodal points c_C and c_D are separating the stable and unstable regions. The binodal points c_A and c_B are given by the common tangent condition $\partial_c \Psi^{\rm con}(c_A) = \partial_c \Psi^{\rm con}(c_B)$. At these points, the configurational energy takes a minimum

T_c and T. The contribution of the configurational energy to the chemical potential will be denoted as $\mu_c = \partial_c \Psi^{\rm con}$.

Further, $\Psi^{\rm sur}(\nabla c)$ denotes the surface energy parameterized in terms of the concentration gradients ∇c. Here we assume a quadratic function for the surface energy

$$\Psi^{\rm sur} = \lambda ||\nabla c||^2, \tag{4}$$

where the parameter λ is related to an internal length scale l as $\lambda = l^2 RT$. Its contribution to the chemical potential takes the following explicit representation, $-\nabla \cdot (\partial_{\nabla c} \Psi^{\rm sur}) = -\lambda \Delta c$. The chemical potential can now be expressed as

$$\mu = \partial_c \Psi^{\rm con} - \nabla \cdot (\partial_{\nabla c} \Psi^{\rm sur}). \tag{5}$$

By inserting these considerations in Eq. (2), we obtain the classical fourth-order diffusion equation which is typically attributed to Cahn and Hilliard [2,3].

$$\dot{c} = \nabla \cdot (M \nabla (\mu_c - \lambda \Delta c)). \tag{6}$$

Remark 1 (*Spinodal decomposition*) The domain of the configurational free energy $\Psi^{\rm con}$ consists of three separate regions, with two convex single-well regions surrounding a non-convex unstable spinodal region at the center. The two points c_C and c_D with $\partial_c^2 \Psi^{\rm con} = 0$ which are separating these regions are called the spinodal points. The two characteristic points c_A and c_B external to the spinodal region and given by the common tangent condition $\partial_c \Psi^{\rm con}(c_A) = \partial_c \Psi^{\rm con}(c_B)$ are called binodal points. At these points, the configurational energy takes a minimum. For particular parameterizations though, $\Psi^{\rm con}$ might have a single well and admit a single phase only. A typical function for the configurational free energy $\Psi^{\rm con}$ for the non convex case is illustrated in Fig. 1.

To complement the strong form of the Cahn–Hilliard equation to an initial boundary value problem, let us consider the domain Ω and its boundary $\Gamma = \partial\Omega$ with an outward unit normal $\boldsymbol{n}$, and let us assume it is sufficiently smooth. We assume the boundary Γ is composed of two complementary parts $\Gamma = \Gamma_c \bigcup \Gamma_t = \Gamma_g \bigcup \Gamma_q$ on which either Dirichlet or Neumann boundary conditions can be prescribed. In the strong form, the problem can be stated as follows. Find $c : \Omega \times (0, \mathcal{T}) \to \mathbb{R}$ such that

$$\nabla \cdot (M \nabla (\mu_c - \lambda \Delta c)) = \dot{c} \quad \text{in } \Omega \times (0, \mathcal{T}) \tag{7a}$$

$$c = \bar{c} \quad \text{on } \Gamma_c \times (0, \mathcal{T}) \tag{7b}$$

$$\nabla c \cdot \boldsymbol{n} = \bar{g} \quad \text{on } \Gamma_g \times (0, \mathcal{T}) \tag{7c}$$

$$M \nabla (\mu_c - \lambda \Delta c) \cdot \boldsymbol{n} = \bar{t} \quad \text{on } \Gamma_t \times (0, \mathcal{T}) \tag{7d}$$

$$M \lambda \Delta c = \bar{q} \quad \text{on } \Gamma_q \times (0, \mathcal{T}) \tag{7e}$$

$$c(x, 0) = c_0(x) \quad \text{in } \Omega \tag{7f}$$

In the above equation, $\dot{c}$ is the temporal evolution of the concentration c. The boundary conditions here are represented in a general form. Equations (7b) and (7c) constitute the Dirichlet boundary conditions on the concentration and its normal gradient. Equations (7d) and (7e) constitute the Neumann boundary conditions. The condition $\nabla_n c = \bar{g}$ on Γ_g has been used in the original derivation of the Cahn–Hilliard equation. These boundary conditions are also evident from the weak form and are discussed in a later section.

Remark 2 (*Degenerate versus constant mobility*) In most physical applications, the mobility M is assumed as $M = D\,c\,[1 - c\,]/[RT]$, where D is the diffusivity which has units of length^2/time. The above relationship for the mobility restricts the diffusion process primarily to the interfacial zones and is commonly referred to as degenerate mobility. This phenomenon is typically observed in physical situations where the movement of atoms is confined to the interfacial region. To simplify the equations, the mobility is often approximated to be constant $M = D/[RT]$.

Remark 3 (*Chemical potential*) The local contribution to the chemical potential $\mu_c = \partial_c \Psi^{\rm con}$ is a highly nonlinear function of the concentration c. It is identical to the potential of a uniform solution in the absence of phase interfaces. In the sequel, we consider a thermodynamically consistent function of the form

$$\mu_c = RT \left[\log \left(\frac{c}{1 - c} \right) + 2\theta \, [1 - 2c] \right]$$

Remark 4 (*Internal length scale*) The parameter $\lambda = l^2 RT$ is a positive constant such that l represents a length scale of

the problem. This length scale is related to the thickness of the interface layer that represents the transition between the two phases. Equations (7) define an appropriate initial boundary value problem for $\lambda > 0$. If $\lambda = 0$, then only Eqs. (7a), (7b) and (7d) are of relevance.

Remark 5 (*Reinterpretation as microforce balance*) In the thermodynamics community, the phase concentration c is typically referred to as order parameter. Accordingly, the fourth-order Cahn–Hilliard equation (7a) can be rephrased as a set of two second-order equations in terms of two order parameters, the conservative concentration field c and another non-conservative field $\tilde{c}$. These fields obey equations that take the form of classical balance equations in continuum thermodynamics with characteristic source and flux terms. In a thermodynamic sense, these two equations can be interpreted as a local microforce balance and a mass balance with associated energy and working performed by the order parameters [18].

Remark 6 (*Dimensionless form of the Cahn–Hilliard equation*) To avoid numerical difficulties associated with different spatial and temporal scales, we rephrase the Cahn–Hilliard equation in a dimensionless form. To this end, we introduce the non-dimensional space and time coordinates $x^* = x/L_0$ and $t^* = t/\mathcal{T}_0$ where L_0 and $\mathcal{T}_0 = {L_0}^4/[D\lambda]$ are the representative length and time scales, respectively. In dimensionless coordinates, the Cahn–Hilliard equation becomes

$$\frac{\partial c}{\partial t^*} = \nabla^* \cdot (M^* \nabla^* (\mu_c^* - \Delta^* c))$$

where $\nabla^* = L_0 \nabla$, $\Delta^* = {L_0}^2 \Delta$, $M^* = M/D$, and ${\mu_c}^* = \mu_c {L_0}^2/\lambda$.

3 The natural element method

The Cahn–Hilliard equation contains spatial derivatives of fourth-order and thus requires an approximation which is at least $\mathcal{C}^1$-continuous. Since classical finite element formulations have well-known difficulties in satisfying higher-order continuity requirements, we pursue a spatial discretization using the natural element method. The natural element method allows an element-free spatial discretization which is entirely node based. It ensures quadratic precision of the interpolant over convex and non-convex boundaries. To illustrate the natural element discretization of the weak form of the Cahn–Hilliard equation corresponding to Eq. (7), we will briefly summarize the natural-element-based interpolation c^{h}. A more detailed description on the implementation of the method for solid mechanics problems can be found in [27] and [7]. Let $c^{\mathrm{h}} \in \mathcal{S}^{\mathrm{h}}$ be the natural element approximation of the concentration field c. In what follows, we demonstrate the derivation of $\mathcal{C}^1$ continuous natural element shape

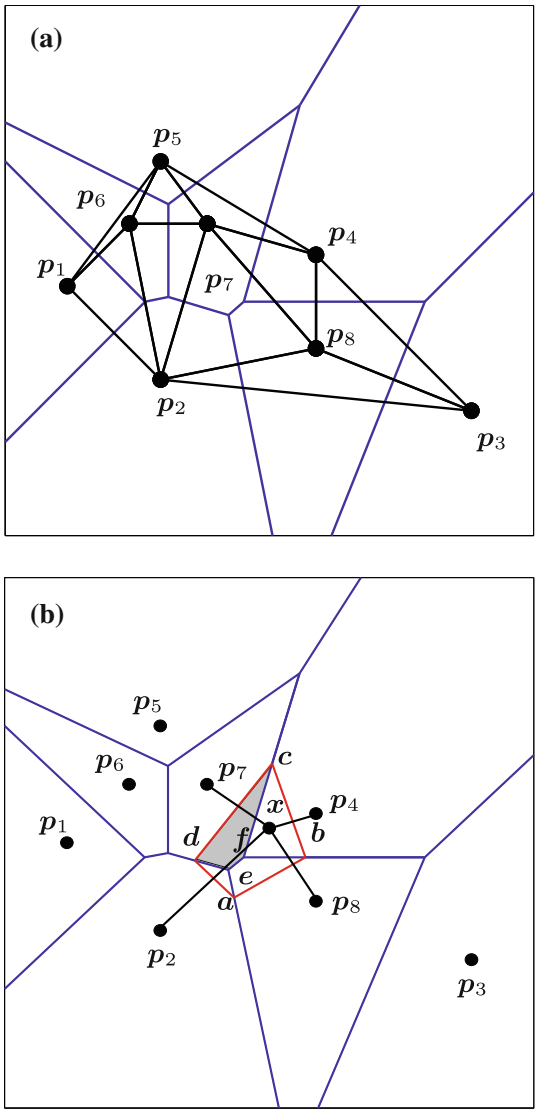

Fig. 2 **a** First-order Voronoi diagram and Delaunay triangulation of a set of points. **b** First-order Voronoi diagram with additional point $\boldsymbol{x}$. The *shaded area* A_{cdef} divided by the area A_{abcd} of the Voronoi cell $\tilde{V}(\boldsymbol{x})$ defines the Sibson interpolant $N_7^0(\boldsymbol{x})$

functions in two steps. First, we illustrate the derivation of $\mathcal{C}^0$-continuous natural neighbor shape functions N^0. Subsequently, we extend the formulation to $\mathcal{C}^1$-continuous natural element shape functions N^1.

3.1 $\mathcal{C}^0$-continuous natural neighbor interpolation

The $\mathcal{C}^0$-continuous natural neighbor interpolants are the Sibsons interpolants, based on the first-order Voronoi diagram. Consider a set of nodes $\mathcal{N} = \{\boldsymbol{p}_1, \boldsymbol{p}_2, \ldots, \boldsymbol{p}_M\} \in \mathbb{R}^d$. The first-order Voronoi diagram $\mathcal{V}(\mathcal{N})$ of the set $\mathcal{N}$ is a subdivision of the Euclidian space $\mathbb{R}^d$ into convex regions $V(\boldsymbol{p}_I) = \{\boldsymbol{x} \in \mathbb{R}^d : ||\boldsymbol{x} - \boldsymbol{p}_I|| < ||\boldsymbol{x} - \boldsymbol{p}_J|| \; \forall J \neq I\}$ called Voronoi cells. The above definition states that any point in the

Voronoi cell $V(\boldsymbol{p}_I)$ is closer to node $\boldsymbol{p}_I$ than to any other node $\boldsymbol{p}_J \in \mathcal{N}$. Figure 2a shows the first-order Voronoi diagram and the corresponding dual Delaunay triangulation for an example consisting of eight node points. Figure 2b illustrates how the natural neighbor interpolant is constructed. For the set of $\mathcal{N}$ nodes considered, the Voronoi diagram is first computed. Now, to interpolate the function value at a arbitrary point $\boldsymbol{x}$, we insert the point $\boldsymbol{x}$ in the set of nodes $\mathcal{N}$ as shown in Fig. 2b. We denote the new nodal set as $\tilde{\mathcal{N}} = \mathcal{N} \cup \boldsymbol{x}$ and the corresponding Voronoi diagram as $\tilde{\mathcal{V}}(\tilde{\mathcal{N}})$. The Voronoi cell of $\boldsymbol{x}$, $\tilde{V}(\boldsymbol{x})$ has k neighboring cells $\tilde{V}(\boldsymbol{p}_1), \ldots \tilde{V}(\boldsymbol{p}_k)$. The k nodes $\boldsymbol{p}_1, \boldsymbol{p}_2, \ldots, \boldsymbol{p}_k$ are called the natural neighbors of $\boldsymbol{x}$. In other words, if $\boldsymbol{x}$ is tessellated along with the nodal set $\mathcal{N}$, then, in the newly constructed triangulation based on $\mathcal{N}$ and $\boldsymbol{x}$, the natural neighbors of $\boldsymbol{x}$ are those nodes that are connected by a Delaunay edge to $\boldsymbol{x}$. The $\mathcal{C}^0$-continuous natural neighbor interpolant N_I^0 about the point $\boldsymbol{x}$, is thus defined as

$$N_I^0(\boldsymbol{x}) := \frac{A(V(\boldsymbol{p}_I) \cap \tilde{V}(\boldsymbol{x}))}{A(\tilde{V}(\boldsymbol{x}))}, \tag{8}$$

where $A(\circ)$ denotes the d-dimensional volume measure. The Sibson interpolants posses properties such as non negativity, $0 \leq N_I^0 \leq 1$, partition of unity, $\sum_I N_I^0 = 1$, interpolation of data, $N_I^0(\boldsymbol{x}_J) = \delta_{IJ}$, allowing the exact imposition of essential boundary conditions, and linear completeness, $\sum_I \boldsymbol{p}_I N_I^0(\boldsymbol{x}) = \boldsymbol{x}$. These interpolants also posses smoothness characteristics such as $\mathcal{C}^\infty$-continuous everywhere except at the nodes and at the boundaries of the support where they are $\mathcal{C}^0$- and $\mathcal{C}^1$-continuous, respectively.

Remark 7 (*Illustration of $\mathcal{C}^0$-continuous shape functions*) To illustrate the geometric interpretation of $\mathcal{C}^0$-continuous natural element shape functions, consider the Voronoi diagram in Fig. 2b. According to Eq. (8), the $\mathcal{C}^0$-continuous natural element shape function $N_I^0(\boldsymbol{x})$ with respect to node $\boldsymbol{p}_7$ is defined as the ratio of the shaded area of overlap of the Voronoi cell $V(\boldsymbol{p}_7)$ to the total area of the Voronoi cell of $\tilde{V}(\boldsymbol{x})$, i.e., $N_7^0(\boldsymbol{x}) = A(V(\boldsymbol{p}_7) \cap \tilde{V}(\boldsymbol{x})) \,/\, \tilde{V}(\boldsymbol{x})) = A_{\text{cdef}} \,/\, A_{\text{abcd}}$. It thus takes the interpretation of the area ratio of the polygons {cdef} and {abcd}.

3.2 $\mathcal{C}^1$-continuous natural neighbor interpolation

To design a $\mathcal{C}^1$-continuous natural neighbor interpolation, we adopt the methodology of generalizing a Bézier patch over a domain. For this we first construct the Farin's interpolant [12] by embedding the $\mathcal{C}^0$-continuous natural neighbor interpolants in the cubic Bernstein–Bézier patch representation of a $(k-1)$-dimensional simplex. The we transform the Bézier ordinates to the nodal degrees of freedom [26]. Let the point $\boldsymbol{x} \in \Omega \subset \mathbb{R}^d$ have k natural neighbors, with $N_I^0(\boldsymbol{x})$ as the natural neighbor shape function of neighbor node I with $I = 1, \ldots, k$. Let us collectively summarize

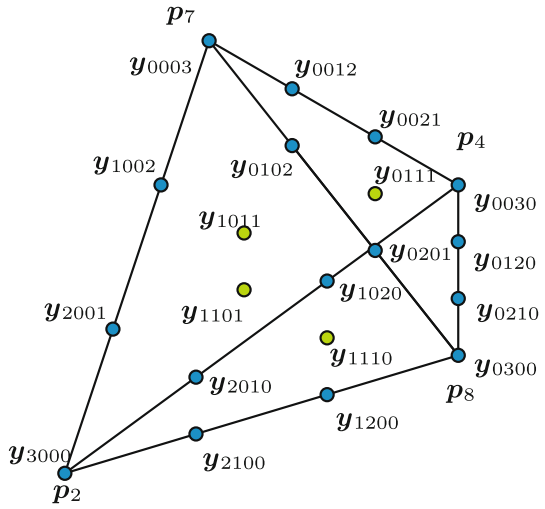

Fig. 3 Projection of the control net of a cubic tetrahedron onto the plane formed by the natural neighbors of node $\boldsymbol{x}$

all $\mathcal{C}^0$-continuous shape functions associated with point $\boldsymbol{x}$ in the vector $\mathbf{N}^0 = [N_1^0(\boldsymbol{x}), N_2^0(\boldsymbol{x}), N_3^0(\boldsymbol{x}), \ldots, N_k^0(\boldsymbol{x})]$. Since $\sum_I N_I^0(\boldsymbol{x}) = 1$, the natural neighbor interpolants $\mathbf{N}^0$ can be considered as barycentric coordinates of a simplex. To obtain the $\mathcal{C}^1$-continuous interpolants, we embed $\mathbf{N}^0$ in a cubic Bernstein–Bézier polynomial, which can be expressed as follows.

$$c^h\left(\mathbf{N}^0\right) = \sum_{|\mathbf{i}|=3} B_{\mathbf{i}}^3\left(\mathbf{N}^0\right) b_{\mathbf{i}} \tag{9}$$

In the above equation, $\mathbf{i}$ denotes a multi-index notation, with the norm $|\mathbf{i}|$ and factorial $\mathbf{i}!$ defined for a cubic case in terms of its components as $|\mathbf{i}| := i_1 + i_2 + \cdots + i_k = 3$ and $\mathbf{i}! := i_1!\, i_2!\, i_3! \ldots i_k!$, respectively. The cubic Bernstein–Bézier basis functions $B_{\mathbf{i}}^3$ can be expressed as $B_{\mathbf{i}}^3(\mathbf{N}^0) = \frac{3!}{\mathbf{i}!}[N_1^0]^{i_1}[N_2^0]^{i_2}, \ldots, [N_k^0]^{i_k}$. Moreover, $b_{\mathbf{i}}$ are the Bézier ordinates associated with the control points $\boldsymbol{y}_{\mathbf{i}} \in \mathbb{R}^d$.

$$\boldsymbol{y}_{\mathbf{i}} = \sum_{|\mathbf{j}|=1} B_{\mathbf{j}}^1\,(\mathbf{i}/3)\,\boldsymbol{p}_{\mathbf{j}} \tag{10}$$

where $\boldsymbol{p}_{\mathbf{j}}$ are the natural neighbor nodes and form the end points of the control net. The control points can be interpreted as the projections of the control net of the cubic Bézier polynomial associated with the $(k-1)$-dimensional simplex onto the plane [11]. For the set of $k = 4$ natural neighbors to point $\boldsymbol{x}$, as shown in Fig. 2b, the projection of the control net of a cubic tetrahedron on to the plane with the corresponding ordinates is shown in Fig. 3. Now, the $\mathcal{C}^1$ interpolants expressed in terms of the Bézier ordinates $b_{\mathbf{i}}$ in Eq. (9) have to be expressed in terms of the nodal values of concentration and gradients of concentration to make them amenable for use in a Galerkin scheme. The vertex Bézier ordinates are equal to the nodal function values of concentration $b_{\mathbf{i}} = c_k$. The tangent Bézier ordinates between

nodes are related to their corresponding nodal gradient values. The remaining Bézier ordinates are related to nodal function and nodal gradient values so as to obtain quadratic completeness. Following the procedure outlined in [26], we can construct a vector $\mathbf{B}$ of Bézier basis functions along with a transformation matrix $\mathbf{T}$ to express the Bézier ordinates in terms of the nodal function values c and nodal gradient values $c_{,x}$ and $c_{,y}$,

$$c^{\mathrm{h}} = \mathbf{B} \cdot \mathbf{b} = \mathbf{B} \cdot \mathbf{T} \cdot \mathbf{c} = \mathbf{N}^1 \mathbf{c}. \tag{11}$$

The transformation matrix $\mathbf{T}$ which maps the nodal function and gradient values $\mathbf{c}$ to the corresponding Bézier ordinates $\mathbf{b}$, as $\mathbf{b} = \mathbf{T} \cdot \mathbf{c}$, is of dimension $[k^2 + \binom{k}{3}] \times [3\,k]$, and the vector of nodal degrees of freedom $\mathbf{c} = [\, c_1, c_{1,x}, c_{1,y}, \ldots, c_k, c_{k,x}, c_{k,y}\,]$ is of dimension $3k$. Thus, using the transformation matrix $\mathbf{T}$, we can construct the $\mathcal{C}^1$-continuous natural element shape functions $\mathbf{N}^1(\boldsymbol{x}) = \mathbf{B}(\mathbf{N}^0(\boldsymbol{x})) \cdot \mathbf{T}$ and express the natural element discretization in a classical format.

$$c^{\mathrm{h}}(\boldsymbol{x}) = \sum_{I=1}^{k} \mathbf{c}_I \cdot \mathbf{N}_I^1(\boldsymbol{x}), \tag{12}$$

Herein, $\mathbf{N}_I^1(\boldsymbol{x}) = [N_{3I-2}^1, N_{3I-1}^1, N_{3I}^1]$ are the cubic shape functions of node I associated with the nodal degrees of freedom $\mathbf{c}_I = [c_{3I-2}, c_{3I-1}, c_{3I}] = [c_I, c_{I,x}, c_{I,y}]$, i.e., the nodal values of the concentration c_I, and the nodal values of their spatial gradients $c_{I,x}$ and $c_{I,y}$.

Remark 8 ($\mathcal{C}^1$*-continuous natural element shape functions*) Most of the properties of the $\mathcal{C}^0$-continuous natural element shape functions and the Bernstein–Bézier patches are inherited by the $\mathcal{C}^1$-continuous shape functions. They thus posses desirable properties such as quadratic completeness and interpolation [26]. Similar to classical cubic Hermitian shape functions, $\mathcal{C}^1$-continuous natural element shape functions interpolate both nodal function values and nodal gradient values

$$\begin{aligned}
&N_{3I-2}^1 \ (\boldsymbol{p}_J) = \delta_{IJ}, \quad N_{3I-1}^1 \ (\boldsymbol{p}_J) = 0, \quad N_{3I}^1 \ (\boldsymbol{p}_J) = 0\\
&N_{3I-2,x}^1 \ (\boldsymbol{p}_J) = 0, \quad N_{3I-1,x}^1 \ (\boldsymbol{p}_J) = \delta_{IJ}, \quad N_{3I,x}^1 \ (\boldsymbol{p}_J) = 0\\
&N_{3I-2,y}^1 \ (\boldsymbol{p}_J) = 0, \quad N_{3I-1,y}^1 \ (\boldsymbol{p}_J) = 0, \quad N_{3I,y}^1 \ (\boldsymbol{p}_J) = \delta_{IJ}.
\end{aligned}$$

This property makes them extremely suitable for the numerical treatment of higher-order partial differential equations such as the Cahn–Hilliard equation. The $\mathcal{C}^1$-continuous natural element shape functions are illustrated in Fig. 4.

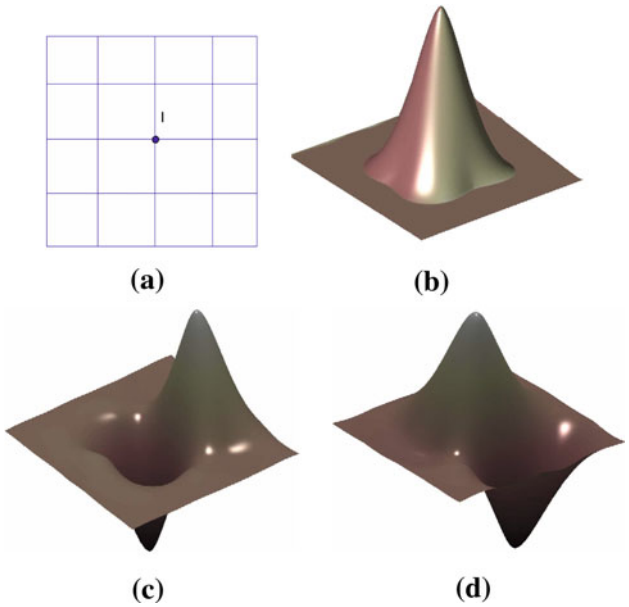

Fig. 4 Illustration of natural element shape functions. **a** Grid, **b** $\mathcal{C}^1$-continuous shape function N_{3I-2} at node I, **c** $\mathcal{C}^1$ shape functions N_{3I-1}, and **d** N_{3I}

4 Numerical formulation

4.1 Weak form of the Cahn–Hilliard equation

Similar to standard Galerkin formulations used in the finite element context, we obtain the integral form of the Cahn–Hilliard equation (7) by multiplication with the test function w and by integration over the domain Ω,

$$R = \int_{\Omega} w\,[\,\dot{c} - \nabla \cdot (\,M\,\nabla\,(\,\mu_c - \lambda \Delta c\,))]\mathrm{d}\Omega \doteq 0. \tag{13}$$

To obtain the symmetric weak form of the residual, we apply the standard integration by parts, once for the second-order term, and twice for the fourth-order term.

$$\begin{aligned}
R = \int_{\Omega} & w\,\dot{c} + \Delta w\,M\,\lambda\,\Delta c\\
&+\nabla w \cdot [M \nabla \mu_c + \nabla M \lambda\,\Delta c]\,\mathrm{d}\Omega\\
&- \int_{\Gamma} w\,M\,\nabla(\mu_c - \lambda\,\Delta c\,) \cdot \boldsymbol{n}\\
&-M\,\lambda\,\Delta c \nabla w \cdot \boldsymbol{n}\,\mathrm{d}\Gamma \doteq 0
\end{aligned} \tag{14}$$

The third and fourth line of the above equation identify the standard and higher-order boundary conditions, respectively, as they appear in the strong form (7). Following the literature, we suggest either periodic Dirichlet or homogeneous Neumann boundary conditions.

4.2 Temporal discretization: trapezoidal method

To discretize the residual equation (14) in time, we use the generalized trapezoidal method. To this end, we partition the time interval of interest into discrete subintervals $[t_n, t_{n+1}]$ with the current increment $\Delta t = t_{n+1} - t_n > 0$. From here on, we omit the index $(n+1)$ for the sake of transparency. We assume that the concentration c_n is known at the beginning of

the time step t_n. Our goal is to find the concentration c at the end of the current time step Δt. The key idea of the generalized trapezoidal method is to update the advancement of the concentration in time, according to the concentration functional $\Pi_\Omega(c, w)$ defined as the functional term of the residual

$$\begin{aligned}\Pi_\Omega(c, w) = &\int_\Omega \Delta w\, M\, \lambda\, \Delta c \\ &+ \int_\Omega \nabla w \cdot [\, M \nabla \mu_c + \nabla M \lambda\, \Delta c\,]\, \mathrm{d}\Omega \\ &- \int_\Gamma w\, M\, \nabla(\mu_c - \lambda\, \Delta c\,) \cdot \boldsymbol{n} \\ &- \int_\Gamma M\, \lambda\, \Delta c \nabla w \cdot \boldsymbol{n}\, \mathrm{d}\Gamma \doteq 0. \end{aligned} \tag{15}$$

Thus in a semi-discretized form, using the generalized trapezoidal method we write

$$\begin{aligned} R_{n+\alpha} = &\int_\Omega w\,[c - c_n]\mathrm{d}\Omega \\ &+\alpha \Delta t\, \Pi_\Omega(c, w) \\ &+[1-\alpha]\Delta t\, \Pi_\Omega(c_n, w) \doteq 0 \end{aligned} \tag{16}$$

It is seen from Eq. (16) that the generalized trapezoidal integration scheme with $\alpha \in [0, 1]$ interpolates the functional Π_Ω rather than the concentration c (which is in contrast to the generalized midpoint rule). The method provides well defined solution values at the end of every time step. Special cases are the Euler backward method with $\alpha = 1$, see e.g. [16,21]; the trapezoidal method with $\alpha = \frac{1}{2}$, see e.g. [25]; and the Euler forward method with $\alpha = 0$.

4.3 Spatial discretization: natural element method

As outlined in Sect. 3, we adopt a natural element interpolation of the test and trial functions c^{h} and w^{h},

$$\begin{aligned} w^{\mathrm{h}}(\boldsymbol{x}) &= \sum_{I=1}^{M} \mathbf{w}_I \cdot \mathbf{N}_I^1(\boldsymbol{x}) \\ c^{\mathrm{h}}(\boldsymbol{x}) &= \sum_{I=1}^{M} \mathbf{c}_I \cdot \mathbf{N}_I^1(\boldsymbol{x}). \end{aligned} \tag{17}$$

where M is the number of nodes. In the above equations, $\mathbf{N}_I^1(\boldsymbol{x}) = [N^1_{3I-2}, N^1_{3I-1}, N^1_{3I}]$ are the natural element shape functions of node I associated with the nodal test function values $\mathbf{w}_I = [w_I, w_{I,x}, w_{I,y}]$ and with the nodal degrees of freedom $\mathbf{c}_I = [c_I, c_{I,x}, c_{I,y}]$. Their gradients can be expressed as follows,

$$\begin{aligned} \nabla w^{\mathrm{h}}(\boldsymbol{x}, t) &= \sum_{I=1}^{M} \mathbf{w}_I \cdot \nabla \mathbf{N}_I^1(\boldsymbol{x}) \\ \nabla c^{\mathrm{h}}(\boldsymbol{x}, t) &= \sum_{I=1}^{M} \mathbf{c}_I \cdot \nabla \mathbf{N}_I^1(\boldsymbol{x}) \end{aligned} \tag{18}$$

where $\nabla \mathbf{N}_I^1(\boldsymbol{x}) = \begin{bmatrix} N^1_{3I-2,x} & N^1_{3I-1,x} & N^1_{3I,x} \\ N^1_{3I-2,y} & N^1_{3I-1,y} & N^1_{3I,y} \end{bmatrix}^t$ is the gradient of the $\mathcal{C}^1$-continuous shape functions. Accordingly, the discrete residual can be expressed as follows,

$$\begin{aligned} \mathbf{R}_I^h = &\int_\Omega \mathbf{N}_I^1\, \frac{1}{\Delta t}[\, c^{\mathrm{h}} - c_n^{\mathrm{h}}\,] + \Delta \mathbf{N}_I^1\, \lambda\, M^{\mathrm{h}}\, \Delta c^{\mathrm{h}} \mathrm{d}\Omega \\ &+ \int_\Omega \nabla \mathbf{N}_I^1 \cdot [\, M^{\mathrm{h}} \nabla \mu_c^{\mathrm{h}} + \nabla M^{\mathrm{h}} \lambda\, \Delta c^{\mathrm{h}}\,] \mathrm{d}\Omega \\ &- \int_\Gamma \mathbf{N}_I^1\, M^{\mathrm{h}}\, \nabla(\mu_c^{\mathrm{h}} - \lambda\, \Delta c^{\mathrm{h}}\,) \cdot \boldsymbol{n} \mathrm{d}\Gamma \\ &- \int_\Gamma M^{\mathrm{h}}\, \lambda\, \Delta c^{\mathrm{h}} \nabla \mathbf{N}_I^1 \cdot \boldsymbol{n} \mathrm{d}\Gamma \doteq \mathbf{0} \end{aligned} \tag{19}$$

where $\Delta \mathbf{N}_I^1 = [N^1_{3I-2,xx} + N^1_{3I-2,yy}, N^1_{3I-1,xx} + N^1_{3I-1,yy}, N^1_{3I,xx} + N^1_{3I,yy}]$ is the discrete Laplacian of the $\mathcal{C}^1$-continuous natural element shape functions. Recall, that the discrete residual in Eq. (19) is a vector-valued expression with three components for each node I, that has to hold for arbitrary nodal test function values, i.e., w_I^{h}, $w_{I,x}^{\mathrm{h}}$, $w_{I,y}^{\mathrm{h}}$.

4.4 Linearization: Newton–Raphson method

For the solution of the highly nonlinear discrete residual statement (19), we suggest an incremental iterative solution strategy embedded in the Newton–Raphson method based on a truncated Taylor series.

$$\mathbf{R}_I^{k+1} = \mathbf{R}_I^k + \mathrm{d}\mathbf{R}_I \doteq \mathbf{0} \quad \text{with} \quad \mathrm{d}\mathbf{R}_I = \sum_{J=1}^{n} \mathbf{K}_{IJ} \cdot \mathrm{d}\mathbf{c}_J \tag{20}$$

By taking into account all the implicit and explicit dependencies through M^{h}, μ_c^{h}, and c^{h} itself, the iteration matrix $\mathbf{K}_{IJ} = \partial \mathbf{R}_I / \partial \mathbf{c}_J$ takes the following explicit representation.

$$\begin{aligned} \mathbf{K}_{IJ} = &\int_\Omega \mathbf{N}_I^1\, \frac{1}{\Delta t}\, \mathbf{N}_J^1 \mathrm{d}\Omega \\ &+ \int_\Omega \Delta \mathbf{N}_I^1\, \lambda [\, M^{\mathrm{h}}\, \Delta \mathbf{N}_J^1 + \Delta c^{\mathrm{h}}\, \partial_c M^{\mathrm{h}}\, \mathbf{N}_J^1\,] \mathrm{d}\Omega \\ &+ \int_\Omega \nabla \mathbf{N}_I^{1\mathrm{t}} \cdot [\nabla \mu_c^{\mathrm{h}}\, \partial_c M^{\mathrm{h}}\, \mathbf{N}_J^1 + M^{\mathrm{h}}\, \partial_c \mu_c^{\mathrm{h}}\, \nabla \mathbf{N}_J^1\,] \mathrm{d}\Omega \end{aligned}$$

$$+\int_{\Omega} \nabla \mathbf{N}_I^{1t} \cdot \lambda[\Delta c^h \, \partial_c M^h \, \nabla \mathbf{N}_J^1 + \nabla M^h \, \Delta \, \mathbf{N}_J^1 \,]\mathrm{d}\Omega$$

$$+\int_{\Omega} \nabla \mathbf{N}_I^{1t} \cdot [\lambda \, \Delta c^h \, \partial_c \nabla M^h \, \mathbf{N}_J^1 + M^h \, \partial_c \nabla \mu_c^h \mathbf{N}_J^1 \,]\mathrm{d}\Omega \tag{21}$$

Recall that iteration matrix $\mathbf{K}_{IJ}$ is a three by three matrix, and the dot product in its definition is taken over the two spatial directions.

Remark 9 (*Degenerate mobility*) For the concentration-dependent degenerate mobility $M = D\,c\,[\,1 - c\,]/[RT]$ advocated in Section 2, the derivative $\partial_c M$ required to evaluate Eq. (21) takes the following format $\partial_c M = D\,[\,1 - 2c\,]/[RT]$.

Remark 10 (*Chemical potential*) For the chemical potential $\mu_c = RT\left[\log\left(\frac{c}{1-c}\right) + 2\theta[1-2c]\right]$ as proposed in Section 2, the derivative $\partial_c \mu_c$ in Eq. (21) can be expressed as follows $\partial_c \mu_c = RT\left[\frac{1}{c\,[1-c]} - 4\theta\right]$. Values of $RT = 1$ and $D = 1$ are assumed for all numerical examples.

Remark 11 (*Stability and accuracy*) The generalized trapezoidal method is flexible time discretization scheme that allows for time discretizations with different orders of accuracy and stability. While for $\alpha = 0$, the method is fully explicit, $\alpha > 0$ characterizes implicit schemes, a typical example of which is the classical trapezoidal rule with $\alpha = \frac{1}{2}$ and the Euler-backward method with $\alpha = 1$. In the context of the Cahn–Hilliard equation discretized with finite element methods, the midpoint method (Crank Nicolson) [30], the trapezoidal rule [25], and the Euler backward method [16,21] have been proposed. In the present manuscript, we adopt the trapezoidal approach with $\alpha = \frac{1}{2}$ and combine it with a heuristic adaptive time stepping procedure. For linear problems, the trapezoidal rule is known to be second-order accurate and unconditionally stable. At large time scales the damping characteristics encountered with the implicit Euler backward scheme are absent in the present method.

Remark 12 (*Adaptive time stepping scheme*) A reliable adaptive time stepping procedure is extremely crucial to efficiently predict the evolution of concentrations using the Cahn–Hilliard equation. The evolution process typically displays rapid variations during the initial phase separation whereas alterations of the concentration field are rather slow during the later stages of Ostwald ripening. We use an adaptive time marching scheme in which the time step size is continuously adjusted based on the convergence behavior of the Newton Raphson iteration. In particular, we divide the current time step size by two if more than six Newton iterations are required to reach the incremental equilibrium state, whereas otherwise, we increase the time step size by 10%. This method has proven extremely powerful in the numerical simulation of all stages of the Cahn–Hilliard equation [21].

5 Examples

5.1 Unit square with constant initial conditions: comparison of different spatial discretizations

A unit square $\Omega = [-0.5, 0.5] \times [-0.5, 0.5]$ domain is considered for simulation using the proposed $\mathcal{C}^1$-continuous natural element method. Periodic boundary conditions are specified on the boundaries. A square subdomain $\Omega_1 = [-0.2, 0.2] \times [-0.2, 0.2]$ is considered with its compliment designated as $\Omega_2 = \Omega \setminus \Omega_1$, the initial conditions for this case are given by

$$c^{\mathrm{ini}}(\boldsymbol{x}, 0) = \begin{cases} 0.71 & \text{for } \boldsymbol{x} \in \Omega_1 \\ 0.69 & \text{for } \boldsymbol{x} \in \Omega_2. \end{cases}$$

These initial conditions are illustrated in Fig. 5. Model parameters of $\theta = 3/2, l^2 = 1/3000$, and a constant mobility with of unit value are considered in the analysis. An initial time step of $\Delta t = 1.7 \times 10^{-7}$ is considered. The degrees of freedom corresponding to the concentration gradients are initialized to zero. Two discretizations of 1057 and 3361 nodes are considered for the analysis. The Voronoi diagrams of these two discretizations are shown in Fig. 5b, c. The initial conditions for these two discretizations are considered identical in a statistical sense. Gaussian quadrature is used for the numerical integration of the discrete residuals (19) and their linearizations (21). The analysis is performed to capture the initial phase separation and a later stationary state of concentrations at which there is no appreciable change in the free energy.

Figures 6 and 7 illustrate snap-shots of the solutions computed for the two discretizations considered in the analysis. The evolution of the concentration can basically be categorized into two phases, a first phase, which is predominantly governed by spinodal decomposition and phase separation, and a second phase which is characterized by grain coarsening. During the first phase, we observe that the concentration is driven into the binodal points in a very fast process. The changes in the concentration are primarily driven by the minimization of the local configurational energy $\Psi^{\mathrm{con}}(c)$. The phase separation period stops as soon as the local concentration takes values of either of the two binodal points. The separation occurs approximately between the times $t = 1.836 \times 10^{-7}$ and $t = 1.462 \times 10^{-6}$. The two discretizations render similar patterns during the initial phase separation. Approximately from $t = 6.645 \times 10^{-6}$ onwards, local changes

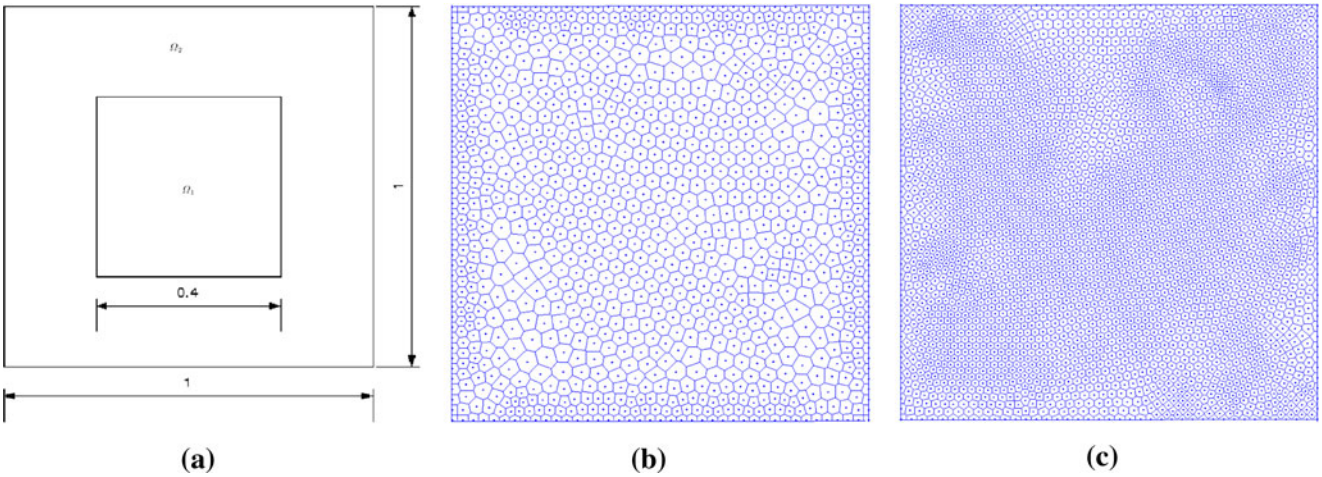

Fig. 5 Box domain and discretization. **a** Initial conditions $c_1^{\text{ini}} = 0.71$ in Ω_1 and $c_2^{\text{ini}} = 0.69$ in Ω_2. **b** Coarse discretization with 1,057 nodes. **c** Fine discretization with 3,361 nodes

in the concentration are primarily governed by the surface free energy $\Psi^{\text{sur}}(c)$. In order to minimize its contribution, the generated patterns cluster and grains tend to coarsen. This phenomenon of Ostwald ripening takes place on a much longer time scale. Grain coarsening is a very slow process and concentrations change between $t = 3.237 \times 10^{-5}$ and $t = 9.782 \times 10^{-5}$. Adaptive time stepping is continued until a stationary state in the concentration is reached, which displays no significant further changes in energy.

A closer look at the concentration history indicates that the evolution of the concentration tends to depend on the spatial discretization. Similar steady state patterns are obtained at all converged stages, indicating that the present formulation gives reasonably good results even for coarser grids. When the grids are too coarse, however, no meaningful results can be obtained. The example was also run for a uniform time stepping scheme. No difference in the results was observed in comparison to the adaptive scheme. This indicates that the concentration evolution is sensitive to the spatial resolution.

Another aspect studied is the ability of the numerical scheme to accurately capture the interface between the two phases.

Recall, that the width of the interface is determined through the parameter $\lambda = l^2 RT$ in the definition of the surface energy (4) where, similar to other higher-order gradient theories, l introduces an internal length scale. Figure 8a, b shows the steady state concentration profile for the discretization comprising of 1,057 and 3,361 nodes respectively. A section $A - A$ from point $[-0.5, 0]$ to $[0.5, 0]$ is considered. Figure 8c shows the corresponding concentration profile along the section $A - A$. We observe that the concentration profiles at the steady state are smooth and the interface is captured well in both coarse and fine discretizations using cubic natural element shape functions. As expected, the smoothness of the interface is more regular in the fine discretization than in the coarse one.

Figure 9a shows the evolution of the free energy, the configurational energy, and the surface energy. The initial phase separation is greatly governed by the large values of configurational energy, whereas the later stages of grain coarsening are governed by the surface energy. Near the stationary condition, at large adaptive time steps, all three energy terms reach a steady state. A comparison of the total free energy for the two discretizations considered is shown in Fig. 9b. The evolution patterns are almost identical for both the discretizations. The slope and smoothness of the curves are greatly determined by the initial value of the concentration. For the assumed initial value closer to one of the energy wells, we obtain a steep and smooth curve as shown in Fig. 9b.

5.2 Unit square with plus-shaped concentration gradient: Comparison of constant and degenerate mobility

A unit square $\Omega = [-0.5, 0.5] \times [-0.5, 0.5]$ domain is considered. A plus-shaped subdomain $\Omega_1 = \Omega_a \cup \Omega_b$ of two rectangular regions $\Omega_a = [-0.25, 0.25] \times [-0.125, 0.125]$ and $\Omega_b = [-0.125, 0.125] \times [-0.25, 0.25]$ is considered inside the unit square, with its compliment designated as $\Omega_2 = \Omega \backslash \Omega_1$ as shown in Fig. 10. Two cases of mobility are considered. In the first case a constant mobility with a unit value is assumed. In the second case a degenerate concentration-dependent mobility defined as $M = c[1 - c]$ is

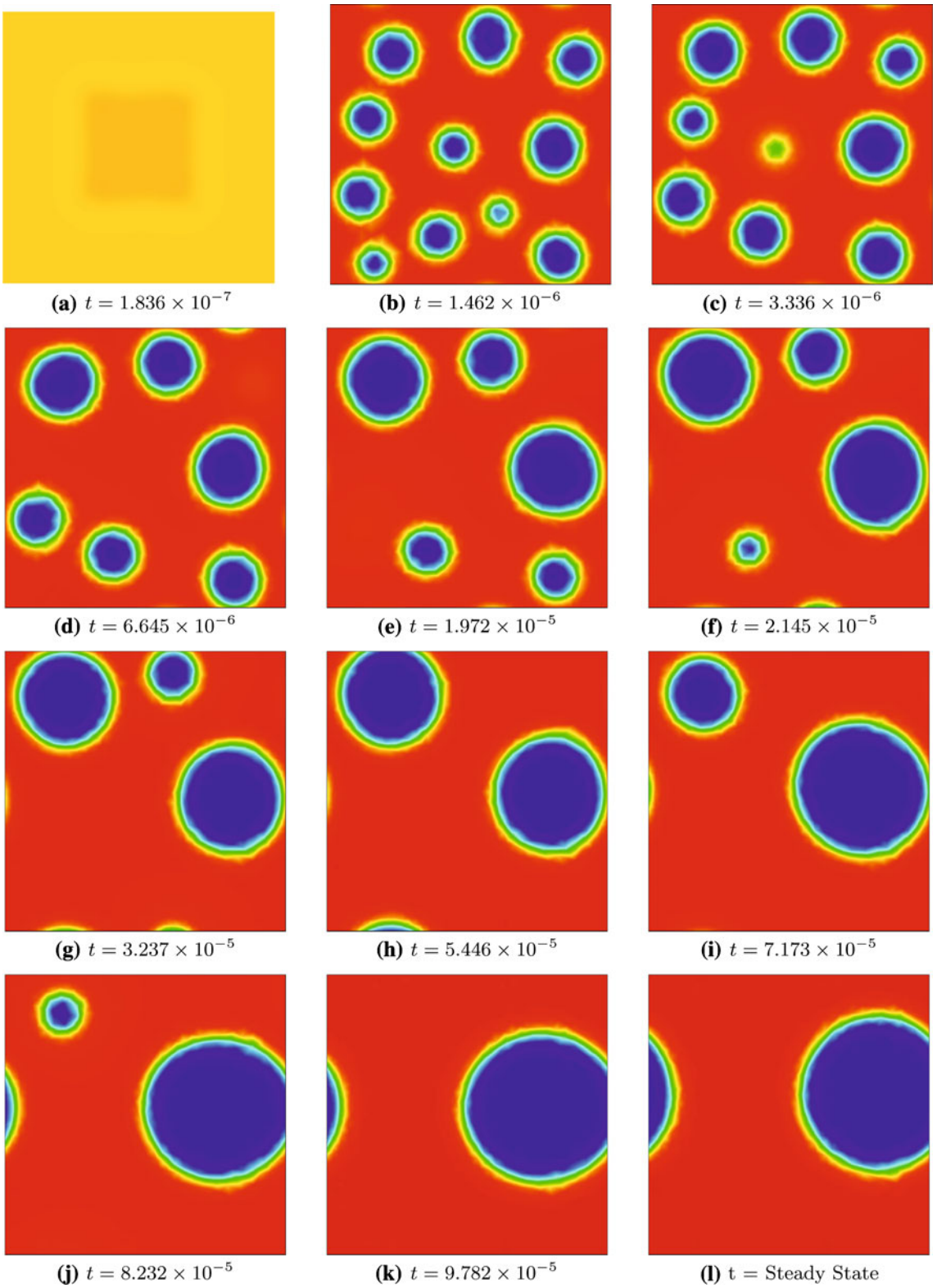

Fig. 6 Spatio-temporal evolution of the concentration from an initial condition of $c_1^{\text{ini}} = 0.71$ and $c_2^{\text{ini}} = 0.69$ for coarse discretization and trapezoidal time integration

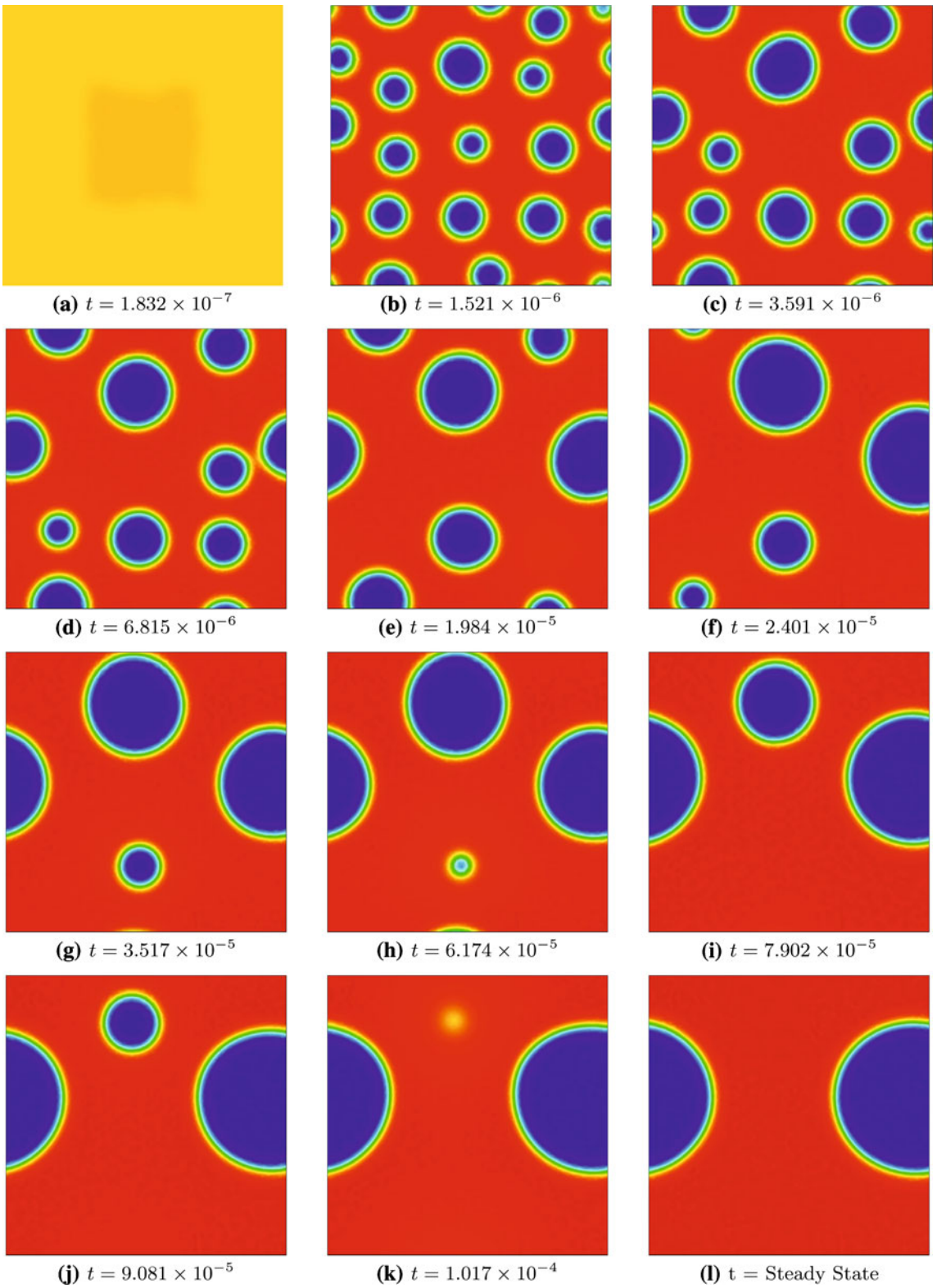

Fig. 7 Spatio-temporal evolution of the concentration from a initial condition of $c_1^{\text{ini}} = 0.71$ and $c_2^{\text{ini}} = 0.69$ for fine discretization and trapezoidal time integration

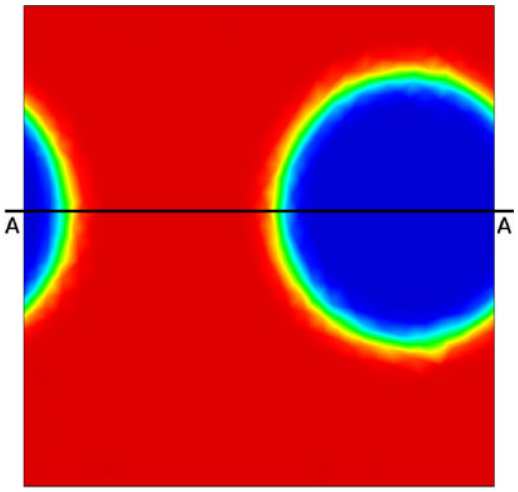

(a)

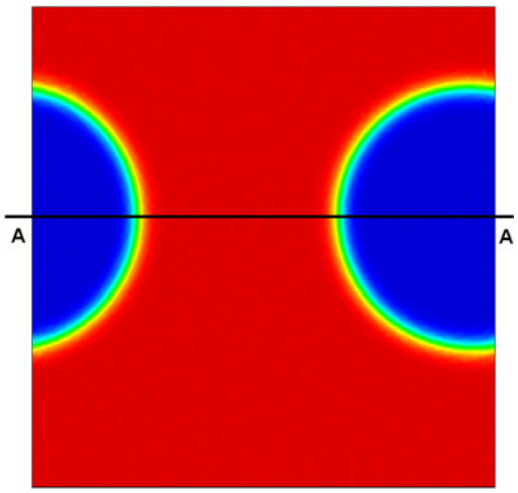

(b)

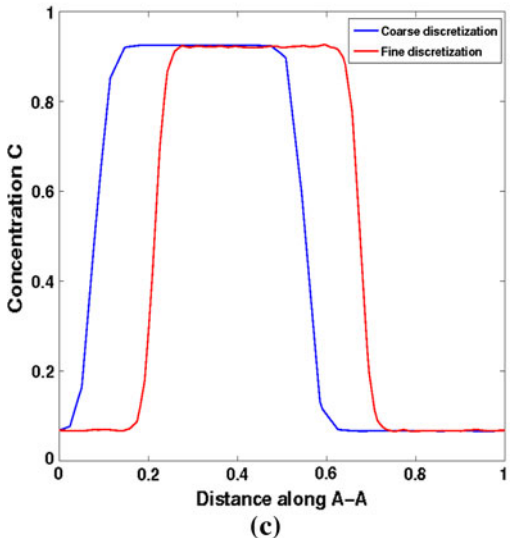

(c)

Fig. 8 Steady state profiles of concentration. **a** Coarse discretization with 1,057 nodes. **b** Fine discretization with 3,361 nodes. **c** Profile of concentration at section $A - A$ for $X = (-0.5, 0)$ to $X = (0.5, 0)$ for coarse and fine discretizations

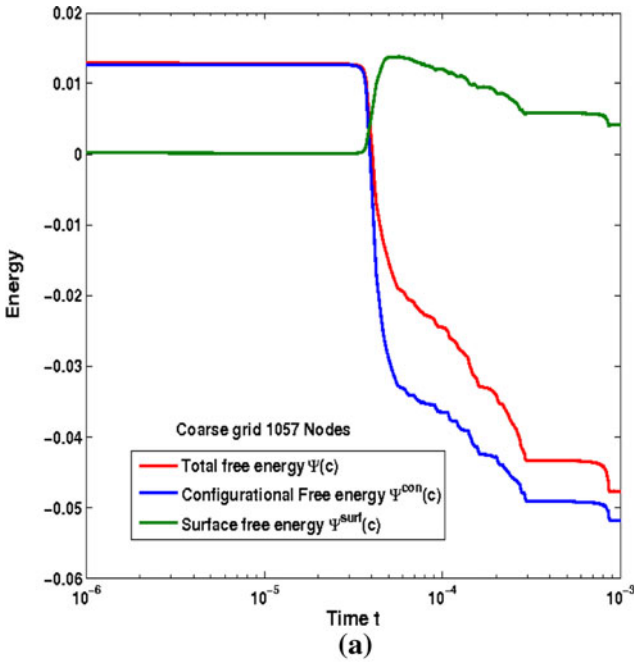

(a)

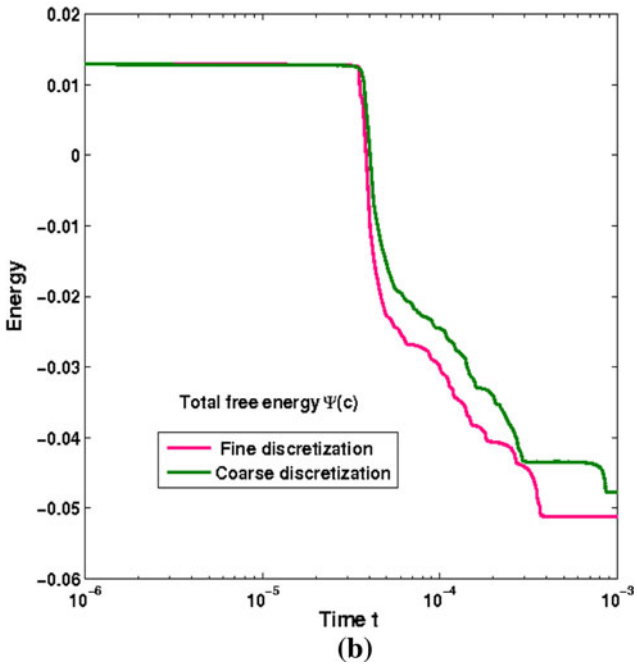

(b)

Fig. 9 Temporal evolution of the total free energy. **a** Evolution of configurational energy, surface energy, and total free energy for fine discretization with 1,057 nodes. **b** Comparison of evolution of total free energy for coarse and fine discretizations

applied. The initial conditions for the constant mobility case are assumed as

$$c^{\text{ini}}(x, 0) = \begin{cases} 0.9 & \text{for } x \in \Omega_1, \\ 0.5 & x \in \Omega_2 \end{cases}.$$

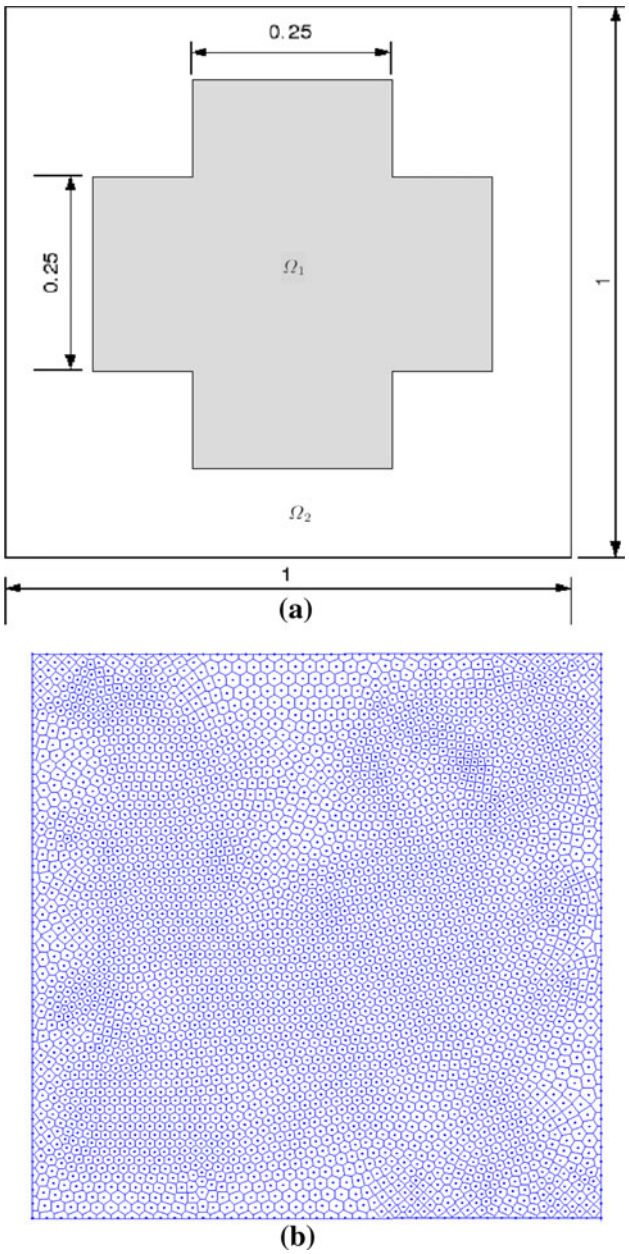

Fig. 10 Plus-shaped domain. **a** Initial conditions $c_1^{\text{ini}} = 0.9$ and $c_2^{\text{ini}} = 0.5$. **b** Voronoi diagram of nodes

For the degenerate mobility case the initial conditions are assumed as

$$c^{\text{ini}}(x,0) = \begin{cases} 0.81 & \text{for } x \in \Omega_1, \\ 0.5 & x \in \Omega_2 \end{cases}.$$

These initial conditions are illustrated in Fig. 10. The model parameters of $\theta = 1.5$, $l^2 = 1/1{,}500$ are considered for both cases. Tables 1 and 2 demonstrate the convergence characteristics of the Newton iterations for the constant mobility and the degenerate mobility case, respectively. For both cases, we achieve the characteristic quadratic convergence. the size of the time steps, and the tolerance used for.

Figure 11 shows the evolution of concentration for the constant mobility case. For the initial concentration values considered, a very fast phase separation is observed between $t = 9.103 \times 10^{-7}$ and $t = 1.051 \times 10^{-5}$. Driven by surface energy minimization, the plus-shaped region evolves in to a circular region as shown in Fig. 11g. Between $t = 1.209 \times 10^{-5}$ and the stationary state the evolution process is characterized by grain diffusion and coarsening. For the present constant mobility case, a steady state solution in the bubble form of two half circles as shown in Fig. 11l is obtained.

Figure 12 documents the evolution of the concentration for the degenerate mobility case. The initial phase separation process is fast and evolution profiles are similar to the constant mobility case. The later stages of grain coarsening are slow and correspond to large adaptive time steps, between 6.734×10^{-5} and 9.473×10^{-5}. A geometric reasoning has been given in earlier works regarding the topology of the steady state solutions of Cahn–Hilliard equation [16]. It has been shown that the free energy converges to the solution of the isoperimetric problem and that the steady state solutions for the constant mobility case are more desirable. For a unit square domain with periodic boundary conditions the solution to the isoperimetric problem is well known, and the minimum configurations are either a bubble or a strip.

5.3 Unit square with random perturbations: influence of different initial concentrations

A unit square $\Omega = [-0.5, 0.5] \times [-0.5, 0.5]$ domain is considered for the analysis. Periodic boundary conditions are specified on all boundaries. For studying the solution of Cahn–Hilliard equation with slight initial inhomogeneities, we assume a concentration of the form

$$c = c^{\text{ini}} + \delta^{\text{pertb}} \quad \text{with} \quad \delta^{\text{pertb}} = \pm 0.045$$

where δ^{pertb} is randomly generated noise. An adaptive implicit Euler backward time stepping scheme based on an initial time step size of $\Delta t = 1.765 \times 10^{-7}$ is considered. Model parameters of $\theta = 3/2, l^2 = 1/3{,}000$ and a constant mobility with unit value are considered for the analysis. In this example, the focus is on studying the influence of the initial concentration on the morphology of the concentration during the phase separation process and at the steady state. Four different initial concentration values of $c^{\text{ini}} = 0.28$, $c^{\text{ini}} = 0.5$, $c^{\text{ini}} = 0.63$ and $c^{\text{ini}} = 0.72$ are considered. We utilize a fine discretization with 3,361 nodes as shown in Fig. 10b.

Table 1 Convergence of residual for unit square domain with plus-shaped concentration gradient with constant mobility

Step 2	Step 10	Step 25	Step 100
$\Delta t = 8.925 \times 10^{-8}$	$\Delta t = 1.487 \times 10^{-7}$	$\Delta t = 2.683 \times 10^{-7}$	$\Delta t = 8.521 \times 10^{-6}$
2.147×10^{1}	6.937×10^{0}	8.261×10^{0}	7.291×10^{0}
1.793×10^{-1}	4.736×10^{-2}	3.472×10^{-2}	4.437×10^{-1}
4.632×10^{-4}	5.107×10^{-4}	3.136×10^{-4}	8.161×10^{-2}
3.763×10^{-7}	8.015×10^{-7}	9.475×10^{-8}	2.431×10^{-4}
8.973×10^{-11}	8.174×10^{-12}	1.184×10^{-11}	1.273×10^{-12}

Table 2 Convergence of residual for unit square domain with plus-shaped concentration gradient with degenerate mobility

Step 2	Step 10	Step 25	Step 100
$\Delta t = 8.925 \times 10^{-8}$	$\Delta t = 1.318 \times 10^{-7}$	$\Delta t = 2.741 \times 10^{-7}$	$\Delta t = 8.392 \times 10^{-6}$
3.181×10^{1}	4.172×10^{0}	2.603×10^{0}	4.590×10^{0}
2.741×10^{-1}	2.315×10^{-3}	7.837×10^{-4}	1.421×10^{-1}
1.712×10^{-5}	6.018×10^{-9}	3.113×10^{-10}	2.504×10^{-4}
4.118×10^{-11}	4.227×10^{-12}	1.194×10^{-14}	3.137×10^{-10}

Similar to the previous examples, we observe that the first stages of the evolution are driven by the minimization of the configurational energy $\Psi^{\text{con}}(c)$ driving the concentrations into the binodal points and resulting in phase separation. Essentially, three types of morphologies are observed during this phase separation phase depending on the initial concentration c^{ini} as shown in Fig. 13. For an initial concentration of $c^{\text{ini}} = 0.28$ and $c^{\text{ini}} = 0.72$ which are both close to either of the energy well regions, we observe a particulate or bubble-type morphology as shown in Fig. 13a, d. For an initial concentration of $c^{\text{ini}} = 0.5$ in the unstable spinodal region, we obtain a co-continuous or worm-type morphology as shown in Fig. 13b. Lastly, for a initial concentration of $c^{\text{ini}} = 0.63$ slightly away from the spinodal region, we observe a combination of both bubble-type and worm-type microstructures are illustrated in Fig. 13c. As expected, the total time required for the phase separation phase indicates that the separation process is much faster near the unstable spinodal region.

Figures 14, 15, 16, and 17 illustrate the spatio-temporal evolution of the concentration field for these four initial conditions, i.e., $c^{\text{ini}} = 0.28$, $c^{\text{ini}} = 0.5$, $c^{\text{ini}} = 0.63$, and $c^{\text{ini}} = 0.72$. Similar to the previous examples, the initial stage of phase separation is followed by long term effects such as clustering of bubbles, bubble diffusion, and growth of bubble- or worm-type morphologies. This process of Ostwald ripening is driven by the minimization of the surface energy and its solution converges towards a stable state at a much larger time scale. The sum of the configurational and surface contribution to the free energy is finally minimized at the illustrated end stages. For the initial concentration values of $c^{\text{ini}} = 0.28$ and $c^{\text{ini}} = 0.72$ lying near either one of the double well regions, we observe from Figs. 14 and 17 that the steady state morphologies correspond to one single bubble. For an initial concentration of $c^{\text{ini}} = 0.63$ slightly away from the spinodal region, the steady state morphology displays one bubbles as shown in Fig. 16. For the initial concentration of $c^{ini} = 0.5$ near the unstable spinodal region, the steady state profile is in the of form a bubble as shown in Fig. 15. In general, the steady state morphology may vary with varying initial random perturbations. Different steady state morphologies are illustrated in Fig. 18.

6 Discussion

In this manuscript, we have proposed the natural element method as a paradigm for the solution of higher-order partial differential equations. In particular, we have focused on the design of a natural-element-based discretization scheme for the Cahn–Hilliard equation. The Cahn–Hilliard equation is a parabolic equation of fourth-order which is characterized through a double-well potential that governs the phase separation of an initially homogeneous mixture, and a surface energy that minimizes the interface between the resulting pure phases. It is this surface energy that introduces fourth-order gradients which require higher-order continuity in the numerical discretization scheme. To construct

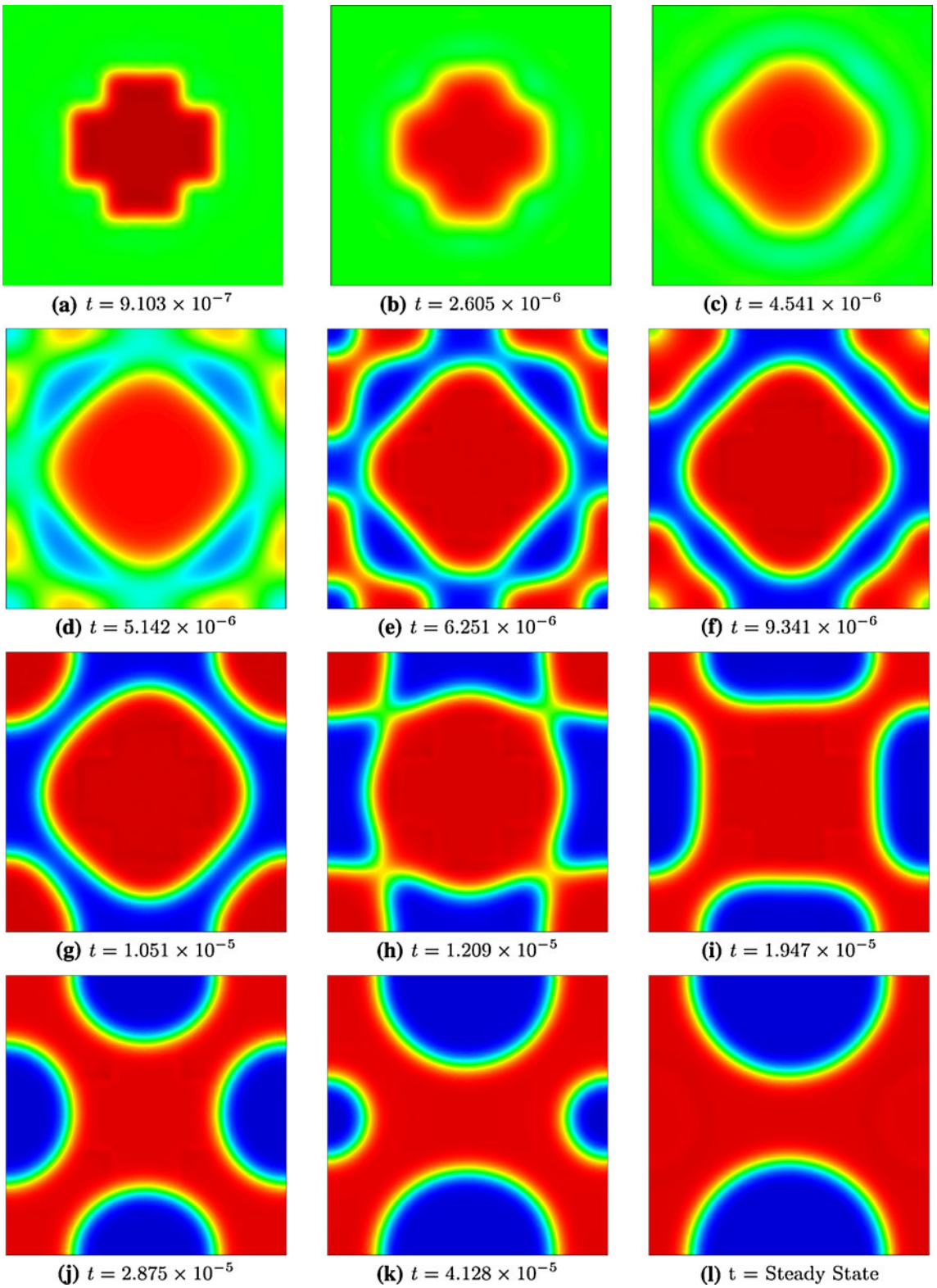

Fig. 11 Spatio-temporal evolution of the concentration for a plus-shaped domain with constant mobility and trapezoidal time integration

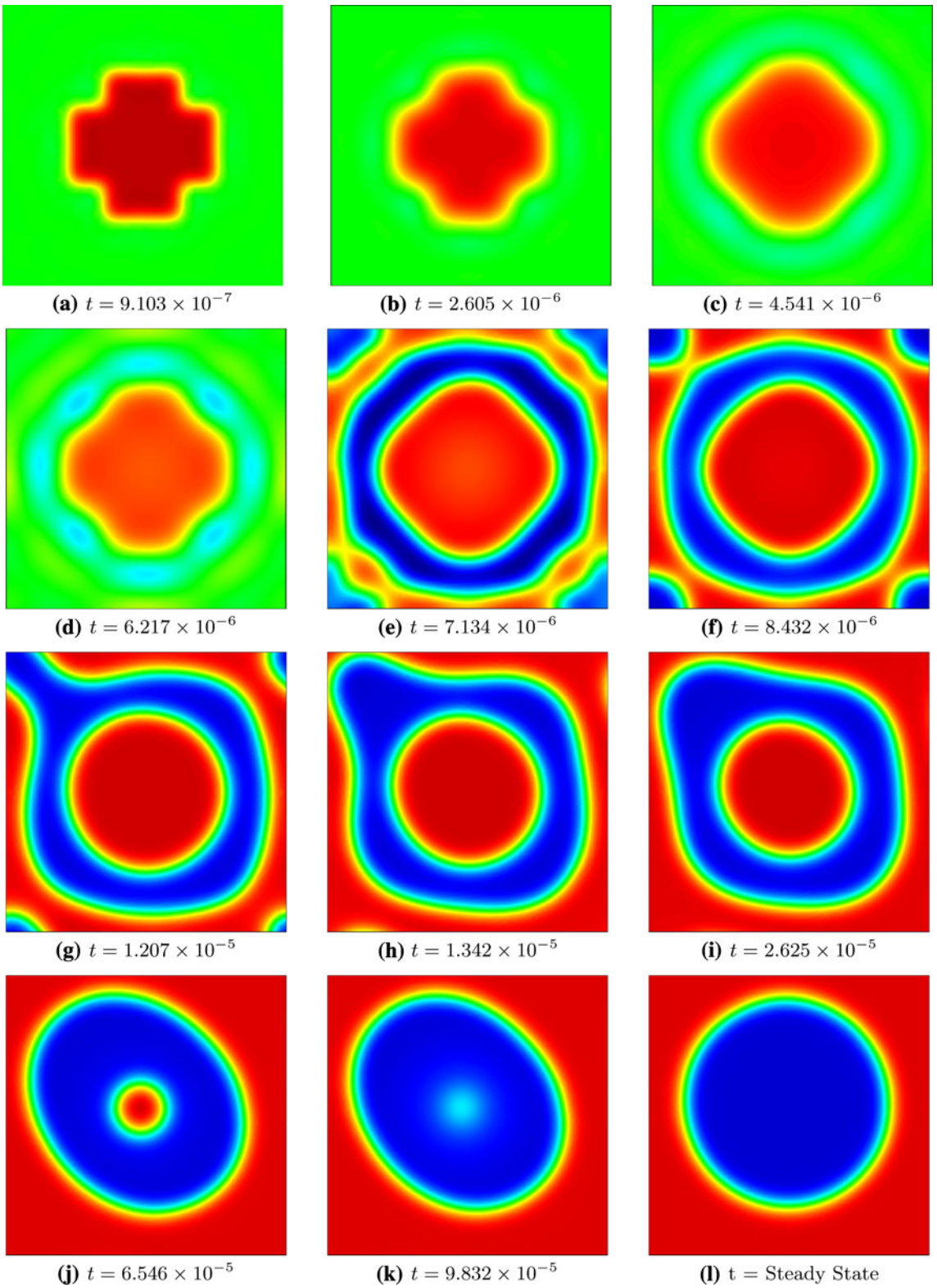

Fig. 12 Spatio-temporal evolution of the concentration for a plus-shaped domain with degenerate mobility and trapezoidal time integration

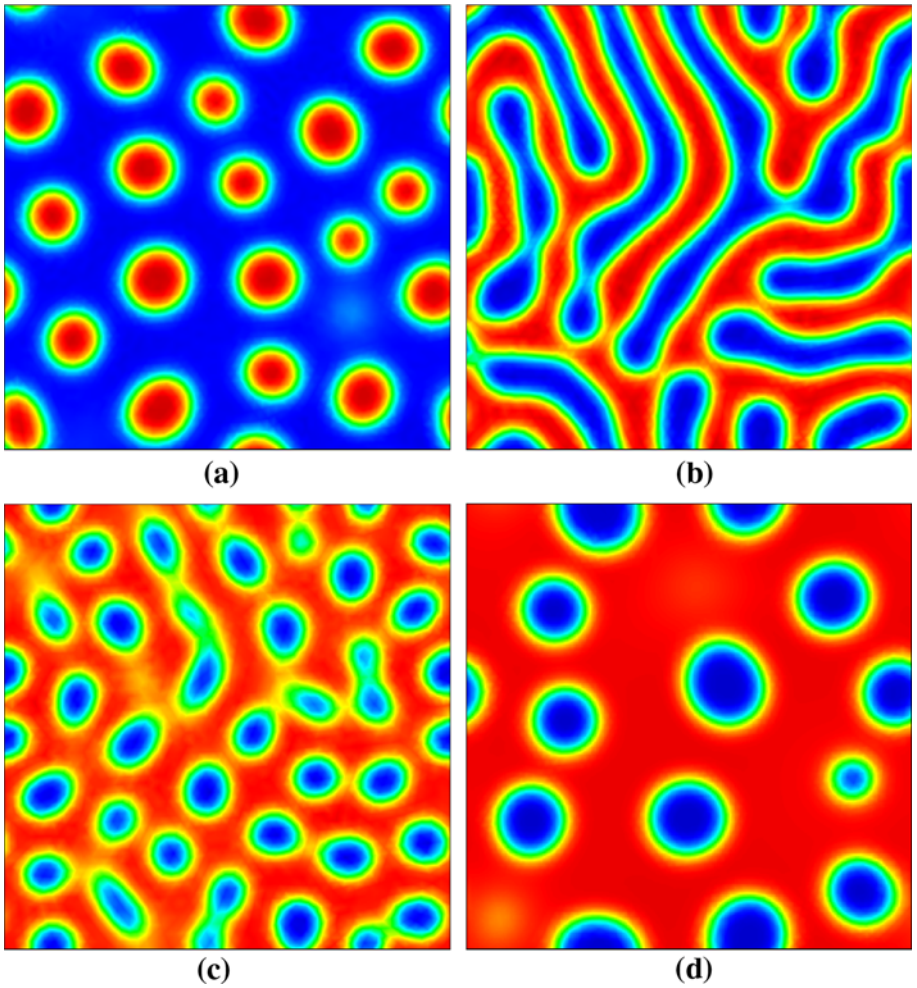

Fig. 13 Influence of initial concentration. **a** $c^{\text{ini}} = 0.28$ at $t = 5.394 \times 10^{-6}$, **b** $c^{\text{ini}} = 0.50$ at $t = 2.213 \times 10^{-6}$, **c** $c^{\text{ini}} = 0.63$ at $t = 9.741 \times 10^{-7}$, and **d** $c^{\text{ini}} = 0.72$ at $t = 5.173 \times 10^{-6}$

shape functions of higher order, we have applied a recently proposed approach in which Bernstein basis functions of the Bernstein–Bézier surface representation of a cubic simplex are transformed into $\mathcal{C}^1$-continuous shape functions that interpolate not only the concentration itself, but also its spatial gradients. Their $\mathcal{C}^1$ interpolation has quadratic completeness, reduces to a cubic polynominal on the domain boundary, and results in classical Hermitian shape functions in one dimension.

The natural element method has several advantages over conventional discretization schemes when solving higher-order differential equations: (i) in contrast to finite difference methods or spectral methods, it is not restricted to regular non-deforming grids; (ii) in contrast to classical $\mathcal{C}^1$-continuous finite element methods, the present method requires fewer degrees of freedom, especially in higher dimensions; (iii) in contrast to nonlocal finite element methods that are based on the discretization of two $\mathcal{C}^0$-continuous fields, it works with exact gradients and not just with their truncated Taylor series' approximation; (iv) in contrast to discontinuous Galerkin methods, it does not require a penalty parameter that ensures the weak enforcement of higher-order continuity requirements.

Applicable to arbitrarily shaped domains, to irregular grids, and to multiple dimensions, the natural element method is computationally efficient, robust, and above all, very flexible. These advantages come at the additional computational cost of having to solve a system of equations not only for the concentration itself, but also for its spatial gradient. The very heart of the method, the computation of the $\mathcal{C}^1$-continuous natural element shape functions, however, involves only basic algebraic matrix-vector operations and does not significantly impact the overall computational cost. In summary, the proposed algorithm has considerable potential, but further mathematical proofs might be needed to rigorously quantify its mathematical characteristics. We believe the natural element method offers an elegant alternative to existing solutions schemes for higher-order differential equations.

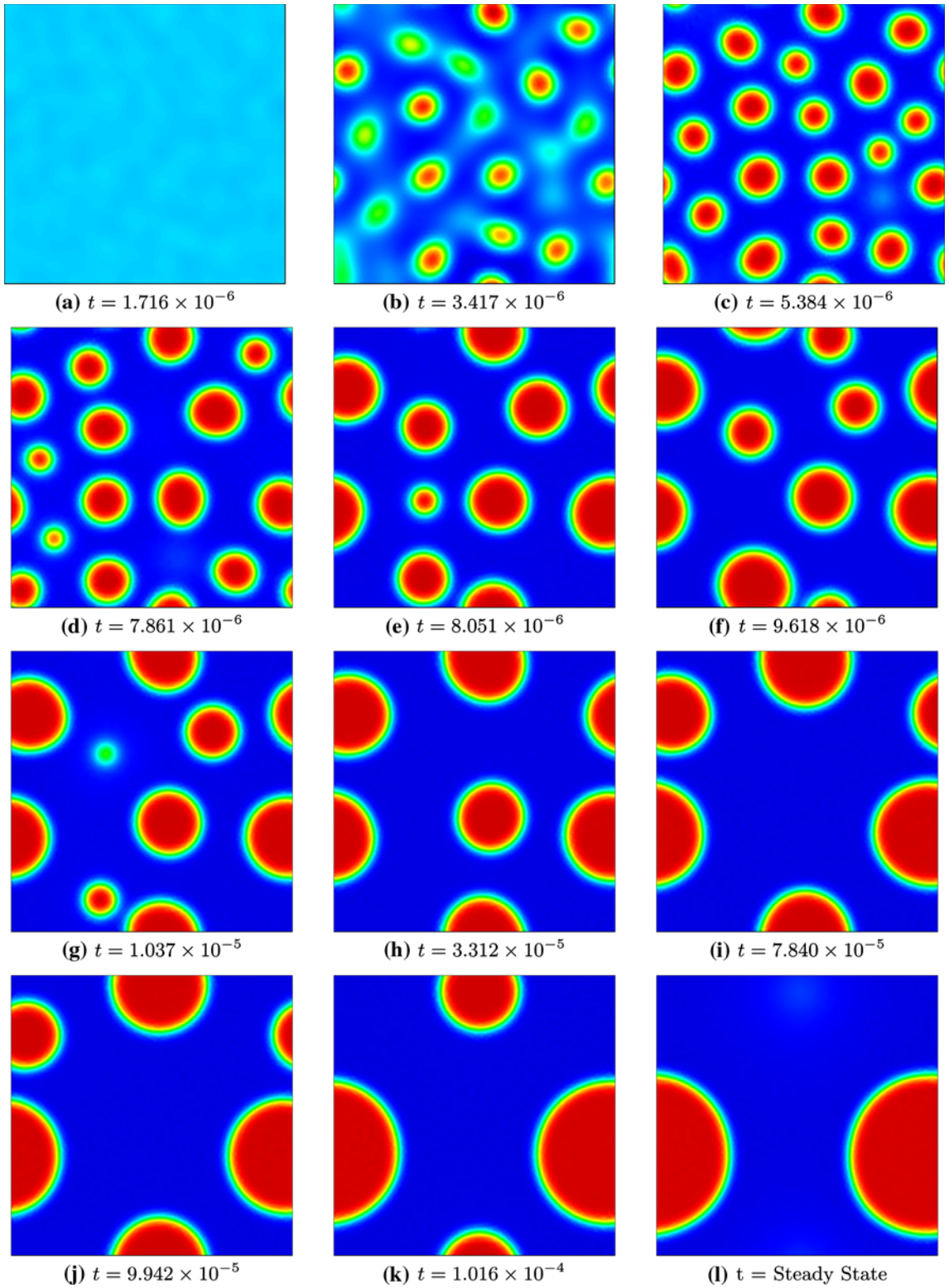

(a) $t = 1.716 \times 10^{-6}$ **(b)** $t = 3.417 \times 10^{-6}$ **(c)** $t = 5.384 \times 10^{-6}$

(d) $t = 7.861 \times 10^{-6}$ **(e)** $t = 8.051 \times 10^{-6}$ **(f)** $t = 9.618 \times 10^{-6}$

(g) $t = 1.037 \times 10^{-5}$ **(h)** $t = 3.312 \times 10^{-5}$ **(i)** $t = 7.840 \times 10^{-5}$

(j) $t = 9.942 \times 10^{-5}$ **(k)** $t = 1.016 \times 10^{-4}$ **(l)** t = Steady State

Fig. 14 Spatio-temporal evolution of the concentration from a randomly perturbed initial condition of $c^{\text{ini}} = 0.28$ and trapezoidal time integration

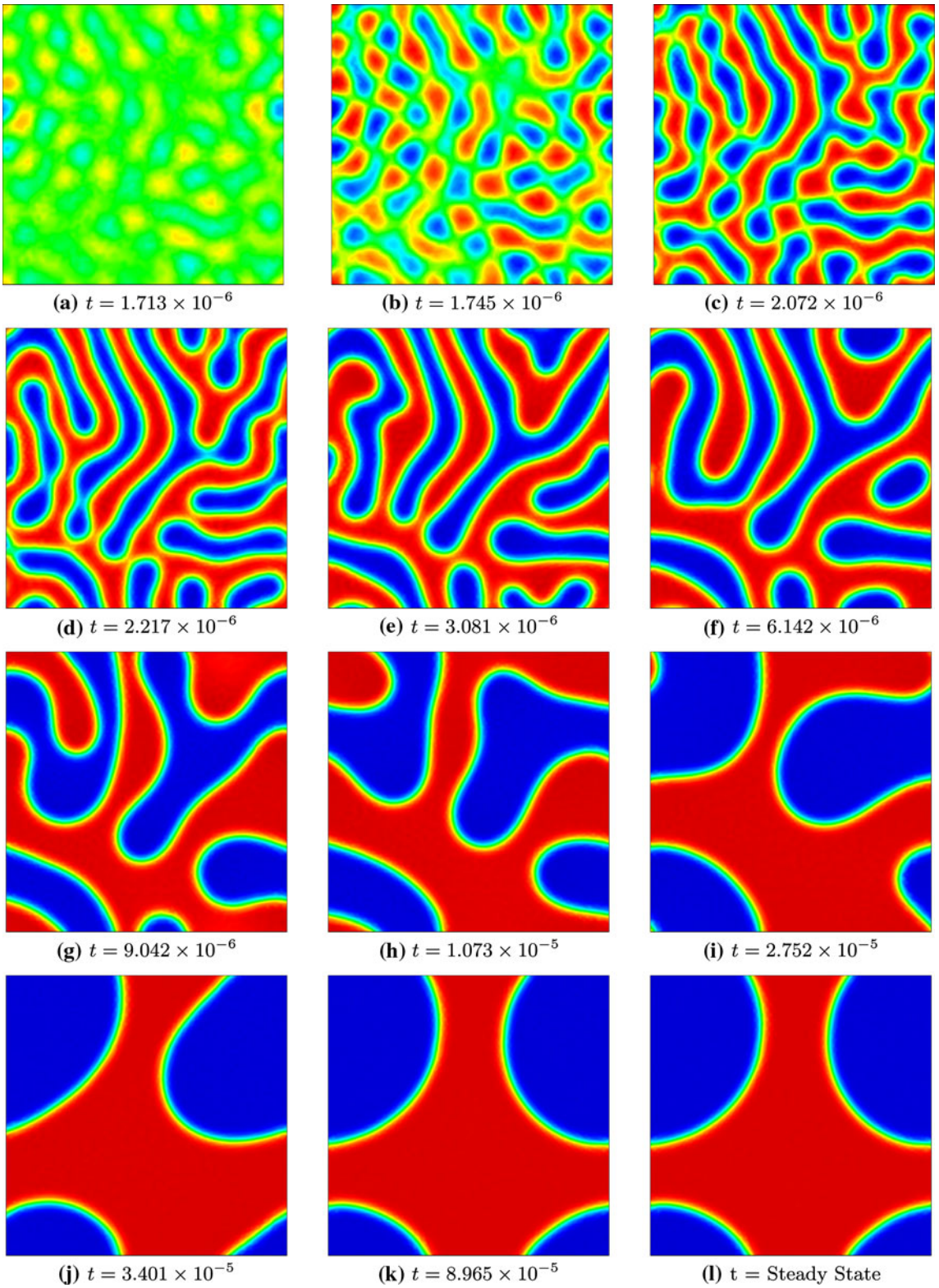

Fig. 15 Spatio-temporal evolution of the concentration from a randomly perturbed initial condition of $c^{\text{ini}} = 0.5$ and trapezoidal time integration

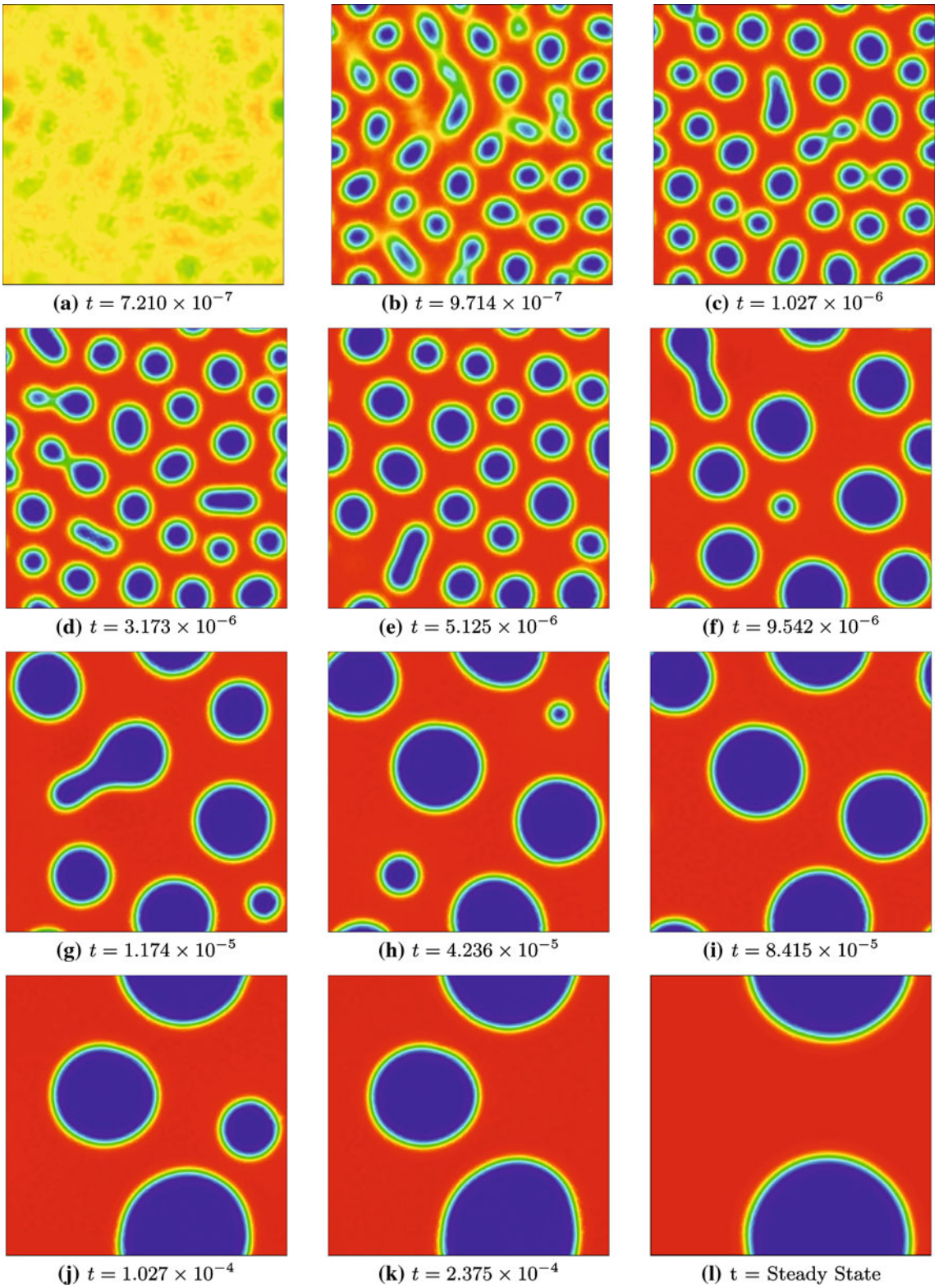

Fig. 16 Spatio-temporal evolution of the concentration from a randomly perturbed initial condition of $c^{\text{ini}} = 0.63$ and trapezoidal time integration

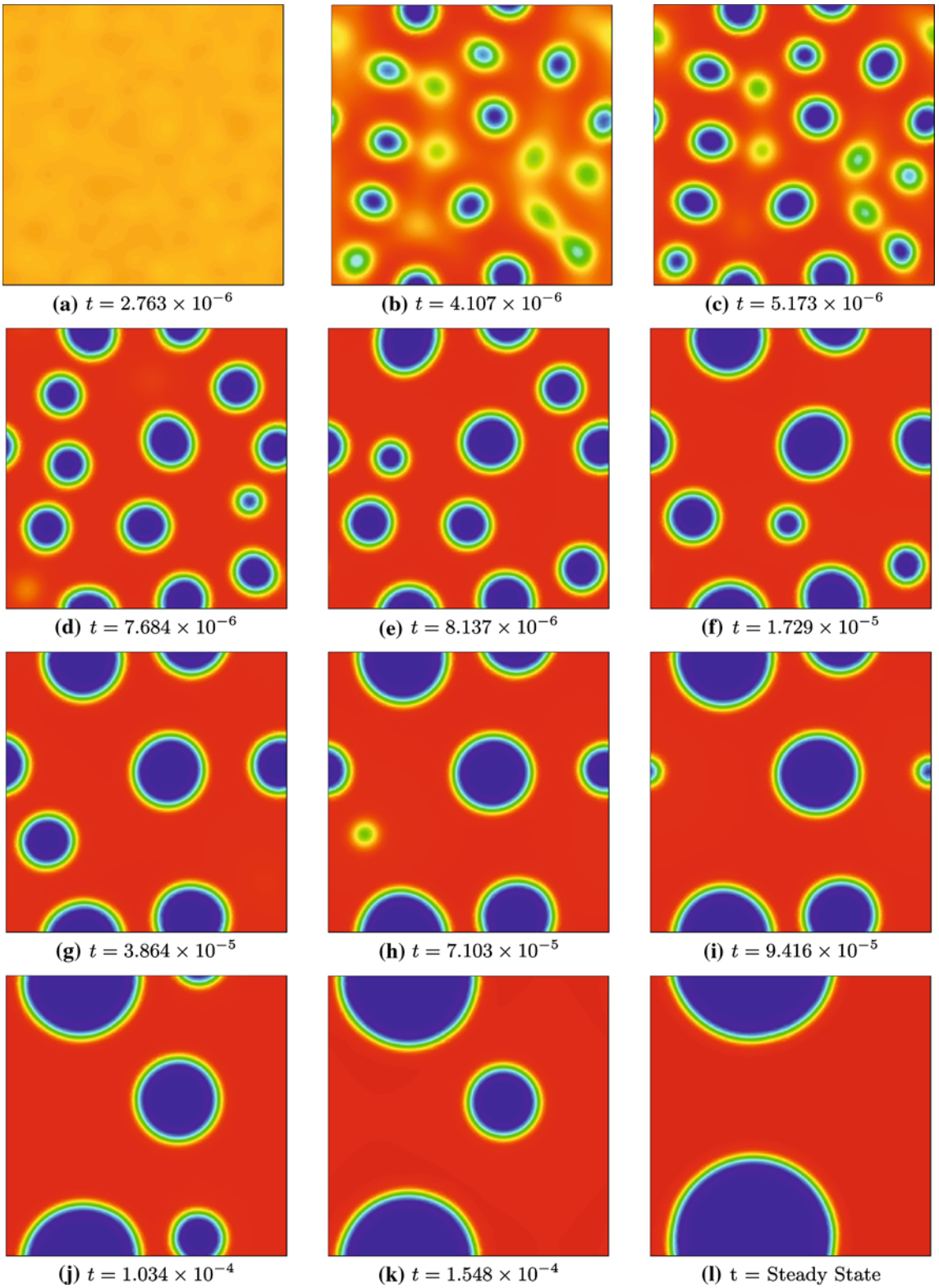

Fig. 17 Spatio-temporal evolution of the concentration from a randomly perturbed initial condition of $c^{\text{ini}} = 0.72$ and trapezoidal time integration

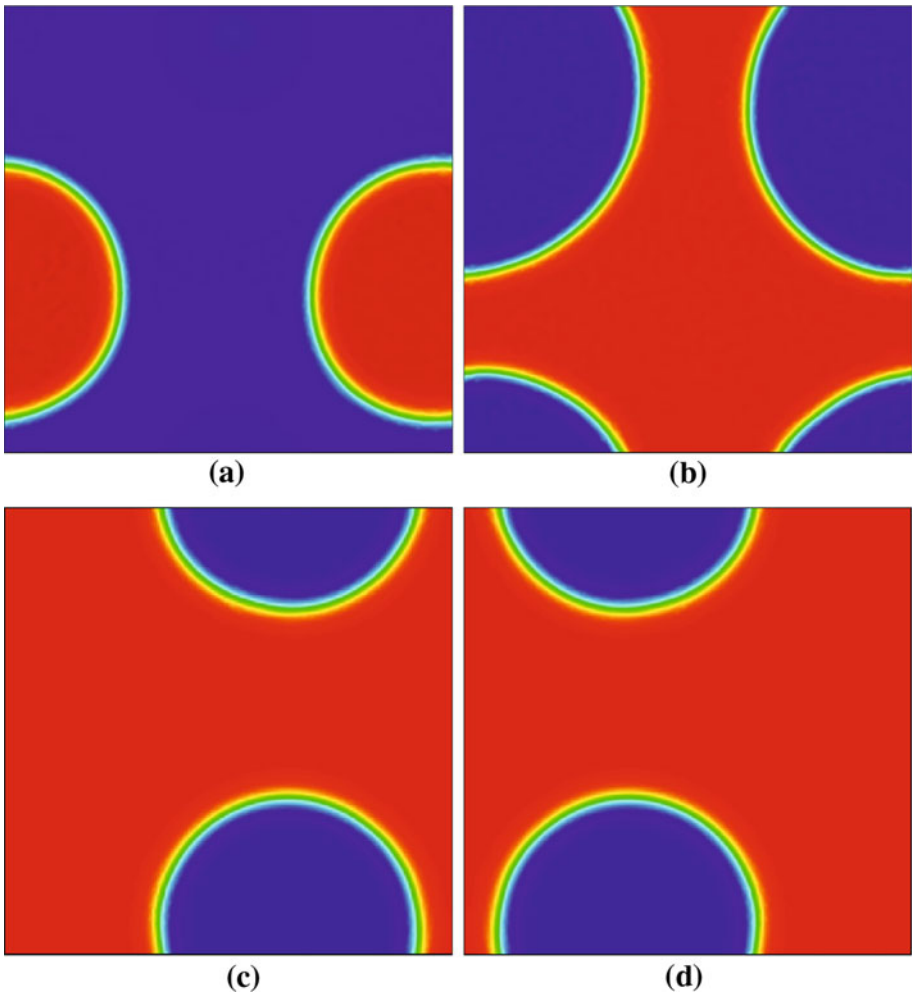

Fig. 18 Different steady state morphologies obtained for different initial concentrations. **a** $c^{\text{ini}} = 0.28$, **b** $c^{\text{ini}} = 0.5$, **c** $c^{\text{ini}} = 0.63$, **d** $c^{\text{ini}} = 0.72$, and varying initial random perturbations δ

Acknowledgments This project is part of the Baravia California Technology Center BaCaTeC Internationalization of High-Tech-Initiative and was initiated during a visit of Paul Steinmann as Timoshenko visiting scholar in the Mechanics and Computation Group of Stanford University. The support of both programs is gratefully acknowledged.

References

1. Barrett JW, Blowey JF, Garcke H (1999) Finite element approximation of cahn hilliard equation with degenerate mobility. SIAM J Numer Anal 37(1):286–318
2. Cahn JW (1959) Free energy of a non uniform system II: thermodynamic basis. J Chem Phys 30:1121–1124
3. Cahn JW, Hilliard JE (1958) Free energy of a non uniform system I: interfacial free energy. J Chem Phys 28:258–267
4. Cahn JW, Hilliard JE (1959) Free energy of a nonuniform system III: nucleation in a two component incompressible fluid. J Chem Phys 31:688–699
5. Choo SM, Chung SK (1998) Conservative nonlinear difference scheme for the Cahn–Hilliard equation—part I. Comput Math Appl 36(7):31–39
6. Copetti MIM, Elliott CM (1992) Numerical analysis of the Cahn–Hilliard equation with a lograthmic free energy. Numer Math 63(1):39–65
7. Cueto E, Sukumar N, Calvo B, Martínez M, Cegoñino J, Doblaré M (2003) Overview and recent advances in natural neighbour Galerkin methods. Arch Comput Methods Eng 10(4):307–384
8. Dolcetta IC, Vita SF, March R (2002) Area preserving curve shortening flows: from phase transitions to image processing. Interfaces Free Boundaries 4(4):325–343
9. Elliott CM, French DA (1989) A non conforming finite element method for the two-dimensional Cahn–Hilliard equation. SIAM J Numer Anal 26(4):884–903
10. Falk F (1992) Cahn–Hilliard theory and irreversible thermodynamics. J Non-Equilibrium Thermodyn 17(1):53–65
11. Farin G (1985) Curves and surfaces for computer aided geometric design. In: Computer science and scientific computing, 4th edn. Academic Press, London
12. Farin G (1990) Surfaces over Dirichlet tesellations. Comput Aided Geom Des 7(1–4):281–292
13. Feng WM, Yu P, Hu SY, Liu ZK, Du Q, Chen LQ (2009) A Fourier spectral moving mesh method for the Cahn–Hilliard equation with elasticity. Commun Comput Phys 5:582–599
14. Fischer P, Mergheim J, Steinmann P (2009) On the C1 continuous discretization of nonlinear gradient elasticity: a comparison of

NEM and FEM based on Bernstein–Bézier patches. Int J Numer Methods Eng. doi:10.1002/nme.2802
15. Furihata D (2001) A stable and conservative finite difference scheme for the Cahn–Hilliard equation. Numer Math 87(4): 675–699
16. Gomez H, Calo VM, Bazilevs Y, Hughes TJR (2008) Isogeometric analysis of Cahn–Hilliard phase field model. Comput Methods Appl Mech Eng 197:4333–4352
17. González D, Cueto E, Doblaré M (2008) Higher order natural element methods: towards an isogeometric meshless method. Int J Numer Methods Eng 74(13):1928–1954
18. Gurtin ME (1996) Generalized Ginzburg-Landau and Cahn–Hilliard equations based on a microforce balance. Physica D 92: 178–192
19. He Y, Liu Y (2008) Stability and convergence of the spectral Galerkin method for the Cahn–Hilliard equation. Numer Methods Partial Differ Equ 24(6):1485–1500
20. Khain E, Sander LM (2008) Generalized Cahn–Hilliard equation for biological applications. Phys Rev E 77(5):1–7
21. Kuhl E, Schmid DW (2007) Computational modeling of mineral unmixing and growth—an application of the Cahn–Hilliard equation. Comput Mech 39:439–451
22. Liu C (2008) On the convective Cahn–Hilliard equation with degenerate mobility. J Math Anal Appl 344(1):124–144
23. Rajagopal A, Scherer M, Steinmann P, Sukumar N (2009) Smooth conformal α-NEM for gradient elasticity. Int J Struct Changes Solids Mech Appl 1(1):83–109
24. Sethian JA (1996) Theroy, algorithms, and applications of level set methods propagating interfaces. Acta Numerica 5:309–395
25. Stogner RH, Carey GF, Murray BT (2008) Approximation of Cahn–Hilliard diffuse interface models using parallel adaptive mesh refinement and coarsening with C1 elements. Int J Numer Methods Eng 76:636–661
26. Sukumar N, Moran B (1999) C^1 natural neighbour interpolant for partial differential equations. Numer Methods Partial Differ Equ 15(4):417–447
27. Sukumar N, Moran B, Belytschko T (1998) The natural element method in solid mechanics. Int J Numer Methods Eng 43(5): 839–887
28. Tryggvason G, Bunner B, Esmaeeli A, Juric D, Al-Rawahi N, Tauber W, Han J, Nas S, Jan YJ (2001) A front tracking method for the computations of multiphase flow. J Comput Phys 169:708–759
29. Ubachs RLJM, Schreurs PJG, Geers MGD (2004) A nonlocal diffuse interface model for microstructure evolution in tin-lead solder. J Mech Phys Solids 52(8):1763–1792
30. Wells GN, Kuhl E, Garikipati K (2006) A discontinious Galerkin method for Cahn–Hilliard equation. J Comput Phys 218:860–877
31. Wu XF, Dzenis YA (2008) Phase-field modeling of the formation of lamellar nanostructures in diblock copolymer thin films under inplanar electric field. Phys Rev E 77(3):1–10
32. Zhou JX, Li ME (2006) Solving phase field equations using a meshless method. Commun Numer Methods Eng 22(11):1109–1115